

Patient-derived organoids from endometrial disease capture clinical heterogeneity and are amenable to drug screening

Matteo Boretto^{1*}, Nina Maenhoudt¹, Xinlong Luo², Aurélie Hennes³, Bram Boeckx^{4,5}, Bich Bui^{1,6}, Ruben Heremans^{1,7,8}, Lisa Perneel¹, Hiroto Kobayashi^{1,9}, Indra Van Zundert¹⁰, Hilde Brems¹¹, Benoit Cox¹, Marc Ferrante¹², Hiroshi Uji-i¹⁰, Kian Peng Koh¹⁰, Thomas D'Hooghe⁷, Arne Vanhie^{3,13}, Ignace Vergote^{7,8}, Christel Meuleman^{3,13}, Carla Tomassetti^{3,13}, Diether Lambrechts^{4,5}, Joris Vriens³, Dirk Timmerman^{7,8} and Hugo Vankelecom^{1*}

Endometrial disorders represent a major gynaecological burden. Current research models fail to recapitulate the nature and heterogeneity of these diseases, thereby hampering scientific and clinical progress. Here we developed long-term expandable organoids from a broad spectrum of endometrial pathologies. Organoids from endometriosis show disease-associated traits and cancer-linked mutations. Endometrial cancer-derived organoids accurately capture cancer subtypes, replicate the mutational landscape of the tumours and display patient-specific drug responses. Organoids were also established from precancerous pathologies encompassing endometrial hyperplasia and Lynch syndrome, and inherited gene mutations were maintained. Endometrial disease organoids reproduced the original lesion when transplanted in vivo. In summary, we developed multiple organoid models that capture endometrial disease diversity and will provide powerful research models and drug screening and discovery tools.

Endometrial diseases are a common gynaecological problem and one of the main causes of infertility^{1,2}. Endometriosis, caused by ectopic growth of endometrium-like tissue, affects 10% of women of reproductive age^{3,4}. The aetiology and pathogenesis are still unclear and the treatment remains unsatisfactory. Endometrial cancer (EC) is the fourth most common type of female cancer⁵. Type I EC, which is oestrogen-dependent, has a favourable prognosis (85% 5-yr survival rate)^{5,6}, while type II EC, which is oestrogen-independent, is frequently high grade with a poorer prognosis (25–60% 5-yr survival rate) and a high risk of metastasis⁵. The clinical management involves surgical resection with chemotherapy and/or adjuvant radiotherapy, but the cancer often recurs⁵. The mechanisms underlying EC pathobiology remain largely unknown and therapy efficiency and overall survival rate are not substantially improving, mainly due to a lack of reliable preclinical study models^{6,7}. The few carcinoma-derived cell lines do not recapitulate clinical EC heterogeneity⁷. Type I low-grade tumours do not successfully grow in vitro, nor in vivo as patient-derived tumour xenografts⁸. Genetic mouse models show aberrations outside the endometrium inconsistent with clinical EC^{7,9}. Finally, study models are not available for precancerous endometrial hyperplasia and

animal models of endometriosis do not closely replicate the typical human disease^{3,10}.

We¹¹ and others¹² recently developed three-dimensional (3D) in vitro organoids from human endometrium that recapitulate key biological features of its epithelium. Here we establish organoid models for endometrial diseases ranging from endometriosis and hyperplasia to low- and high-grade cancer. The organoids show long-term expandability, genomic and transcriptomic stability and replicate disease diversity. Our study initiates an endometrial organoid biobank encompassing both healthy and pathological conditions, thereby providing promising preclinical study models and drug screening and discovery tools.

Results

Patient biopsies (Supplementary Table 1) were seeded in optimized culture conditions to generate 3D organoids that were amplified for multiple passages, subjected to downstream analyses and cryopreserved for biobanking (Supplementary Fig. 1a).

Establishment of long-term expandable organoids from endometriotic lesions. In endometriosis patients, endometrium-like

¹Laboratory of Tissue Plasticity in Health and Disease, Stem Cell and Developmental Biology Cluster, Department of Development and Regeneration, KU Leuven, Leuven, Belgium. ²Stem Cell Institute Leuven, Department of Development and Regeneration, KU Leuven, Leuven, Belgium. ³Laboratory of Endometrium, Endometriosis and Reproductive Medicine, Department of Development and Regeneration, KU Leuven, Leuven, Belgium. ⁴Center for Cancer Biology, VIB, Leuven, Belgium. ⁵Laboratory for Translational Genetics, Department of Human Genetics, KU Leuven, Leuven, Belgium. ⁶Woman and Baby Division, Reproductive Medicine, University Medical Centre Utrecht (UMCU), Utrecht, The Netherlands. ⁷Woman and Child Cluster, Department of Development and Regeneration, KU Leuven, Leuven, Belgium. ⁸Gynecology and Obstetrics, University Hospitals Leuven (UZ Leuven), Leuven, Belgium. ⁹Department of Anatomy and Structural Science, Faculty of Medicine, Yamagata University, Yamagata, Japan. ¹⁰Laboratory of Molecular Imaging and Photonics, Department of Chemistry, KU Leuven, Leuven, Belgium. ¹¹Laboratory for Neurofibromatosis Research, Department of Human Genetics, KU Leuven, Leuven, Belgium. ¹²Unit of Translational Research in Gastrointestinal Disorders, Department of Chronic Diseases, Metabolism and Ageing, KU Leuven, Leuven, Belgium. ¹³Leuven University Fertility Center (LUFC), UZ Leuven, Leuven, Belgium. *e-mail: matteo.boretto@kuleuven.be; hugo.vankelecom@kuleuven.be

tissue grows at ectopic sites such as the peritoneum and ovary³. Endometriosis samples (Supplementary Table 1) were cultured as previously defined for healthy endometrium¹¹ (with minor modifications; see Methods and Supplementary Table 2). Organoids (referred to as ectopic organoids (ECT-O); Supplementary Fig. 1a) developed within 7–14 d, although at a lower number than organoids from healthy endometrium (EM-O; Fig. 1a,b and Supplementary Fig. 1b) and at a lower efficiency (Fig. 1c), which may be due to the harsher dissociation conditions required for endometriotic tissue resulting in poorer yield. ECT-O could also originate from single cells (Supplementary Fig. 1c). The organoids displayed substantial proliferation (Fig. 1d) and could be expanded long-term in a similar way to EM-O (Fig. 1e and Supplementary Fig. 1d). Organoids could be established from all ectopic implantation sites and from the different American Society for Reproductive Medicine revised staging system (rASRM)¹³ clinical stages (I–IV, defined according to the location, number, infiltration and adhesions of the lesions; Supplementary Fig. 1e and Supplementary Table 1). Long-term expandable organoids were also generated from the eutopic endometrium of endometriosis patients, generating patient-matched eutopic organoids (EUT-O) and ECT-O (Fig. 1a–c,e, Supplementary Fig. 1a,b,d and Supplementary Table 1). The ECT-O displayed genomic stability during long-term expansion (Fig. 1f) and this was also confirmed for EM-O and EUT-O (Supplementary Fig. 1f). In addition, transcriptomic stability was found as analyzed for several endometrial markers (Supplementary Fig. 1g).

Next, we tested the requirement of multiple medium compounds for the growth of ECT-O (as compared to EM-O). The WNT signal amplifier RSPO1 was necessary for efficient organoid growth (Fig. 1g)¹¹. WNT pathway inhibition with IWP2 (ref. 14; in the absence of RSPO1) significantly reduced growth (Fig. 1g and Supplementary Fig. 1h), thus indicating endogenous WNT signalling. Organoid growth could be rescued by RSPO1, WNT3A and WNT7A but not by the non-canonical WNT5A (ref. 14; Supplementary Fig. 1h). WNT5A and WNT7A were the most expressed WNT ligands in the ECT-O (Supplementary Fig. 1i; as previously found in EM-O¹¹). Expression analysis of WNT target genes further supported the involvement of the canonical pathway¹⁴ (Supplementary Fig. 1h). The omission of EGF significantly impaired both ECT-O and EM-O expansion, while the removal of Noggin compromised ECT-O growth (Fig. 1g).

ECT-O recapitulate disease phenotype in vitro and in vivo. In general, the ECT-O contained a lumen-bordering cell layer that was thicker than in the EM-O and EUT-O (Supplementary Fig. 2a and Supplementary Videos 1 and 2). Several ECT-O displayed luminal invasion as found in primary lesions (Fig. 2a and Supplementary Fig. 2a), in line with the expression of matrix metalloproteinase(s) (MMP) (Supplementary Fig. 2b). Endometriotic tissue exhibited estrogen receptor α (ER α) and progesterone receptor (PR) expression, which was retained in the organoids (Fig. 2a), while pancyokeratin (PanCK) and E-cadherin confirmed their epithelial nature (Fig. 2a and Supplementary Fig. 2c). Primary lesions secreted mucus in their lumina, which was also recapitulated in ECT-O (periodic acid–Schiff (PAS) staining; Fig. 2a), indicating the presence of secretory cells and polarization, the latter further supported by the presence of laminin at the basolateral side (Fig. 2a) and of microvilli and cilia directed towards the lumen (Fig. 2b and Supplementary Fig. 2d). Transmission electron microscopy (TEM) confirmed the stratified epithelium in ECT-O, which was not observed in EM-O and EUT-O (Fig. 2b and Supplementary Fig. 2d). In addition, TEM showed the presence of non-ciliated secretory cells with secretory vacuoles (Fig. 2b, dashed box).

Next, we investigated whether ECT-O could in vivo generate grafts that reproduce endometriotic features. After subrenal transplantation, ER α ⁺ and PR⁺ lesions developed (Supplementary

Fig. 2e). Given the prevailing peritoneal location of endometriotic lesions, ECT-O were injected into the peritoneal cavity and this generated implants expressing endometriotic markers (Fig. 2c).

Transcriptomic and genetic analyses of ECT-O reveal disease-associated traits. RNA-sequencing (RNA-seq) analysis of ECT-O, EUT-O and EM-O revealed type-specific differentially expressed genes (Fig. 3a, Supplementary Fig. 3a,b and Supplementary Tables 3–5). Principal component analysis (PCA) showed a general clustering of EM-O and EUT-O but more variation within and within the ECT-O samples (Supplementary Fig. 3a) that may, at least partly, be due to their different lesion type and rASRM stage (Supplementary Table 1). Gene ontology analysis identified altered pathways and biological terms in the ECT-O (as compared to the EM-O; Supplementary Tables 6 and 7). In particular, extracellular matrix (ECM)-receptor interaction genes (for example, *COL3A1*, *FN1*, *ITGA11*, *LAMA2*), PI3K–AKT signalling pathway genes (for example, *IGF1*, *ITGB8*, *PDGFR*), WNT pathway genes (for example, *CTNNA2*, *LEF1*, *WNT11*), hormonal response genes (for example, *HSD11B1*, *LIFR*, *PGR*, *PRLR*), Hippo signalling genes (for example, *CTGF*, *GDF7*) and adhesion and invasion genes (for example, *MMP2*, *SNAI2*, *TIMP4*) showed altered expression levels (Fig. 3a, Supplementary Fig. 3b and Supplementary Tables 6 and 7). These adhesion/invasion factors are important for the anchorage and growth of tissue at ectopic sites and have been previously associated with endometriosis^{15–20}. Moreover, *HOXD8* and *HOXA9*, both essential in female reproductive tract development^{20,21}, were upregulated in ECT-O (Fig. 3a and Supplementary Fig. 3b). Contrasting EUT-O with EM-O has the potential to identify pathway differences in the endometria of endometriosis patients and healthy women. For instance, the downregulation of *BAMBI* and the upregulation of *GDF11* in EUT-O (Fig. 3a and Supplementary Fig. 3b) may suggest increased transforming growth factor- β pathway activity in patient endometrium.

Because rASRM stages I–IV were not equally represented in the RNA-seq analysis (Supplementary Table 1), thus precluding stage-specific profiling, we performed reverse transcription–quantitative PCR (RT–qPCR) analysis (as compared to EM-O) on multiple organoid lines from individual endometriosis stages for a selection of genes (including RNA-seq hits). A prominent finding was the upregulation of *LEF1*, *WNT11* and *LGR6* (the latter particularly in the higher stages III–IV, in which deep lesions are predominant; Fig. 3b,c and Supplementary Fig. 3c). In addition, we identified significant downregulation of the progesterone-regulated gene *PAEP* and increased expression of *LIFR* and of the candidate endometrium stem cell marker *SOX9*, all in line with previous findings in endometriosis²² (Fig. 3d). *MMP2* is significantly upregulated in stages II and IV (with clinical mild to strong invasion of ovarian/deep lesions) while inflammatory cytokines *IL-1 β* and *IL-8* are predominantly upregulated in stage I–II ECT-O (Supplementary Fig. 3d), in accordance with endometriosis establishing as an inflammatory disease²³. Comparing matched ECT-O and EUT-O from individual patients identified *LGR6* as one of the top upregulated genes in the ectopic tissue organoids (Supplementary Fig. 3e,f and Supplementary Table 4).

Finally, we performed whole-exome sequencing (WES) on a selected number of ECT-O lines with either low or high rASRM staging. A *KRAS* hotspot mutation (G12V) was identified in the stage IV ECT-O₁₃ line (Fig. 3e), which was confirmed in the corresponding RNA-seq data (by single-nucleotide polymorphism (SNP) variant calling). Additional aberrations were found in EC-associated driver genes in stage IV but not stage I ECT-O. Particularly, we identified potential somatic mutations in *CTCF*, *EP300* and *ZNF471* (Fig. 3e). Recent studies also found mutations in EC-associated genes in endometriotic (ovarian and deep) lesions^{24,25}.

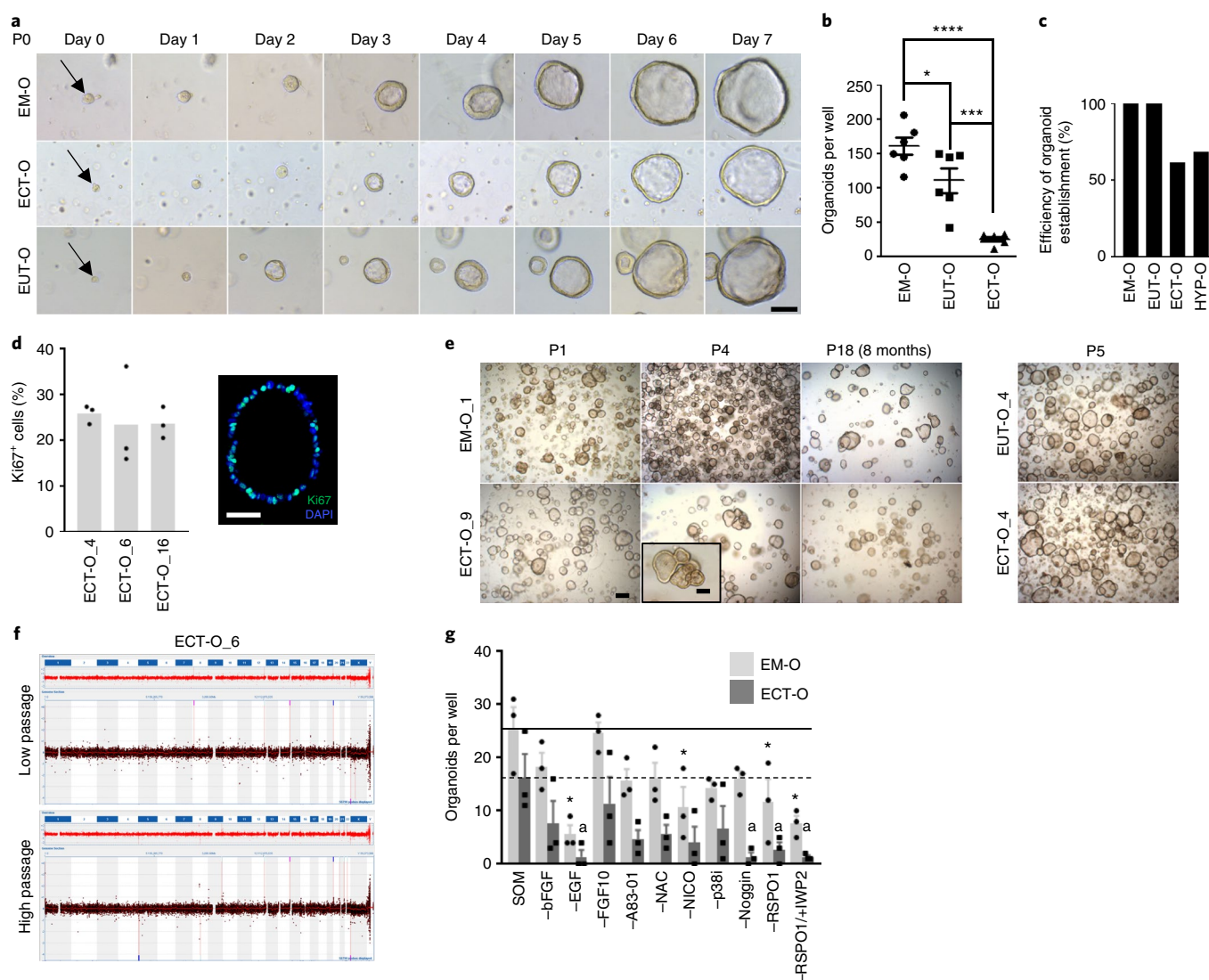


Fig. 1 | Long-term expandable organoids can be established from endometriosis. **a**, Brightfield images of EM-O, ECT-O and EUT-O after seeding (P0). Arrows indicate the specific tissue subunit monitored in time. Representative images from three independent experiments (three independent donors per endometrial condition) are shown. Scale bar, 50 μ m. **b**, The formation efficiency (PO) of EM-O, EUT-O and ECT-O (horizontal lines and error bars show the mean number of organoids formed \pm s.e.m. of $n=6$ biologically independent experiments). **** $P < 0.0001$, *** $P < 0.001$, * $P < 0.05$; one-way analysis of variance (ANOVA). **c**, The efficiency of organoid establishment from the different endometrium conditions (percentage of total biopsies seeded; $n=15$ EM-O, $n=15$ EUT-O, $n=21$ ECT-O and $n=11$ HYP-O). **d**, A proliferation analysis of ECT-O: the quantification of Ki67⁺ cells in organoids from three independent donors as indicated (left; bars show the mean of three technical replicates per donor) and Ki67 immunofluorescence (right; a representative image of three independent experiments (three donors); 4,6-diamidino-2-phenylindole (DAPI) was used as the nuclear stain). Scale bar, 50 μ m. **e**, Brightfield images of different passages demonstrating the long-term expansion of EM-O and ECT-O (left; a representative structure is magnified in the inset) and of matched EUT-O and ECT-O from an individual patient (right). Representative images of three independent experiments (three independent donors per condition) are shown. Scale bars, 200 μ m in the overview images and 50 μ m in the inset. **f**, aCGH plots of ECT-O from low (1–2 months) and high (4–6 months) passage numbers. SCNA were absent and this was maintained during long-term culture. Representative plots of three independent experiments (three independent donors) are shown. **g**, Analysis of medium factor requirements for the growth of EM-O (as compared to growth in standard organoid medium (SOM), indicated by the solid line) and ECT-O (as compared to growth in SOM, indicated by the dashed line). Organoids were cultured in the absence of the indicated compounds (individually omitted from the SOM) for 7 d and the organoid number determined (bars and error bars show the mean \pm s.e.m. of $n=3$ biologically independent experiments, each performed in triplicate). * $P < 0.05$ among EM-O as compared to SOM, ^a $P < 0.05$ among ECT-O as compared to SOM; one-way ANOVA. EGF, epidermal growth factor; FGF, fibroblast growth factor; bFGF, basic fibroblast growth factor; NAC, N-acetyl-L-cysteine; NICO, nicotinamide; P, passage.

Organoids from endometrial precancer pathologies recapitulate disease phenotype and genetics. Endometrial hyperplasia often precedes cancer development^{6,26}. Using the culture conditions defined above (Supplementary Table 2), we were able to establish organoids from hyperplastic endometrium (HYP-O) (70% efficiency; Fig. 1c) originating from three different subtypes: simple

benign, complex atypical and polyp (Fig. 4a, Supplementary Fig. 4a and Supplementary Table 1). The organoids showed considerable proliferative activity (Fig. 4b) and could be long-term passaged (for more than 6 months; Fig. 4a). The HYP-O displayed a stratified PanCK⁺ epithelium lining a central lumen (Fig. 4c and Supplementary Fig. 4b). Molecular and subcellular features of

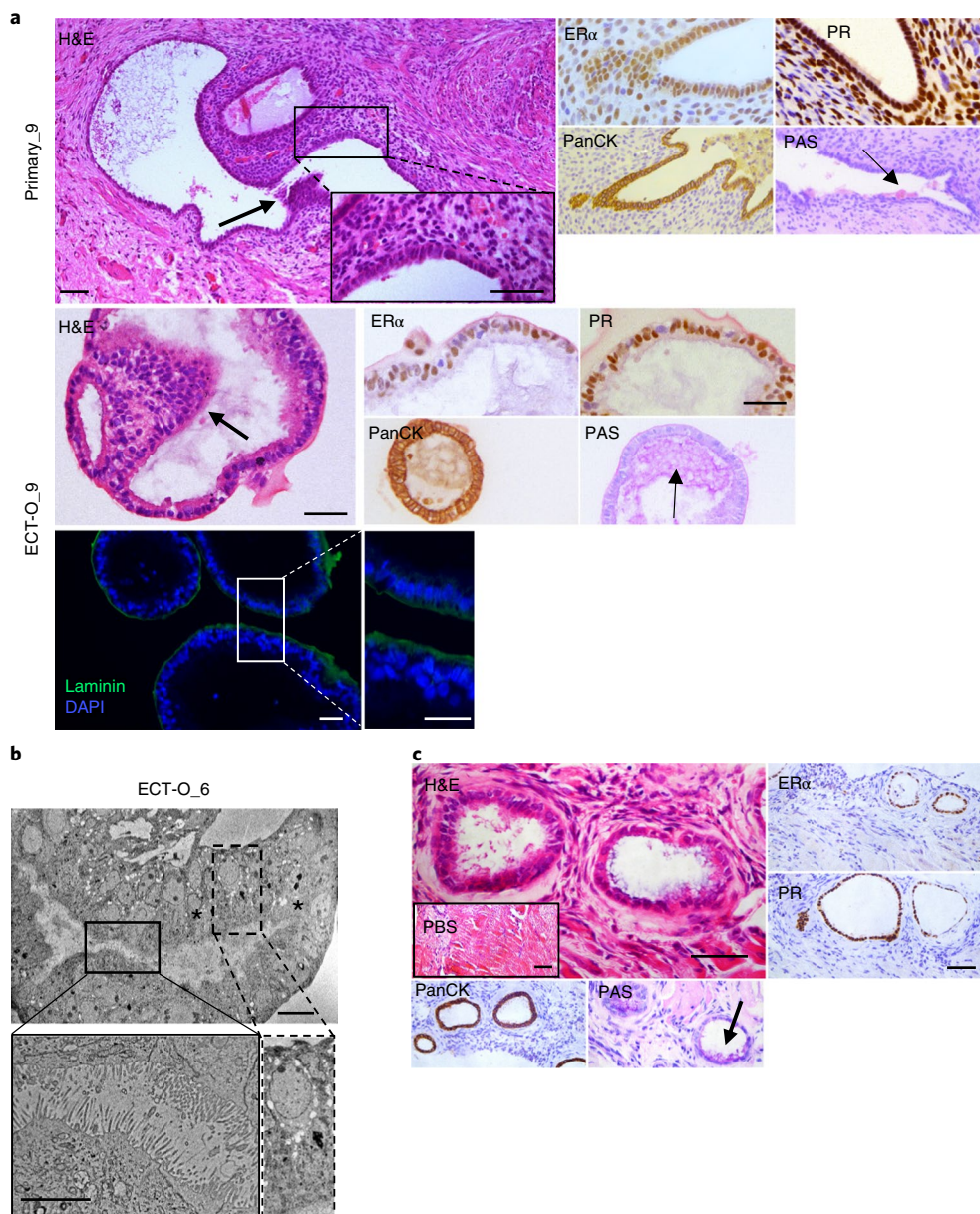


Fig. 2 | ECT-O reproduce the primary lesion in vitro and in vivo. a, Histological (haematoxylin and eosin (H&E)) analysis, immunohistochemical examination of endometrial markers and mucin detection (PAS staining) in primary endometriotic peritoneal lesions and corresponding organoids (ECT-O) and immunofluorescence analysis of laminin in organoids. Arrows point to the invasive phenotype (H&E) or to mucin production (PAS). Boxed areas are magnified as indicated. Representative images of five independent experiments (five independent donors) are shown. Scale bars, 50 μ m. **b**, A TEM image revealing glandular-like morphology, stratified epithelium (asterisks) and the presence of microvilli and cilia (solid box) and non-ciliated secretory cells with secretory vacuoles (dashed box) in ECT-O. The boxed areas are magnified as indicated. Representative images of three independent experiments (three independent donors) are shown. Scale bars, 10 μ m. **c**, Representative H&E analysis, immunohistochemical examination for endometrial markers and mucin detection (PAS; arrow) in peritoneal engraftments of ECT-O 2 months after intraperitoneal injection ($n=4$ biologically independent experiments). Inset: H&E staining of sham (PBS-injected) mice that did not grow any lesions. Scale bars, 50 μ m.

primary tissue (such as the presence/absence of P53 and mucus) were faithfully recapitulated in the HYP-O (Supplementary Fig. 4b,c). No somatic copy number alterations (SCNAs) were found in the primary biopsies and corresponding organoids (Supplementary Fig. 4d).

Lynch syndrome is an inherited predisposition to cancer, primarily developing in the colon and endometrium²⁷. Patients typically harbour mutations in DNA repair genes²⁷. We were able to derive long-term expandable organoids from endometrium hyperplasia biopsies of Lynch syndrome patients (Fig. 4d). Targeted resequencing

showed that the specific mutations affecting mismatch repair (MMR) genes (*MSH2* and *MSH6*) were retained in the corresponding organoids (Fig. 4e).

EC-derived organoids (EC-O) capture disease heterogeneity. We generated organoids from different grades and progression stages of EC (Supplementary Table 1). EC-O developed in 7–20 d (Supplementary Fig. 5a,b). However, efficiency was considerably lower (20%; Fig. 5a) than for the other endometrial conditions (Fig. 1c) and organoids showed limited expansion potential. Moreover, in

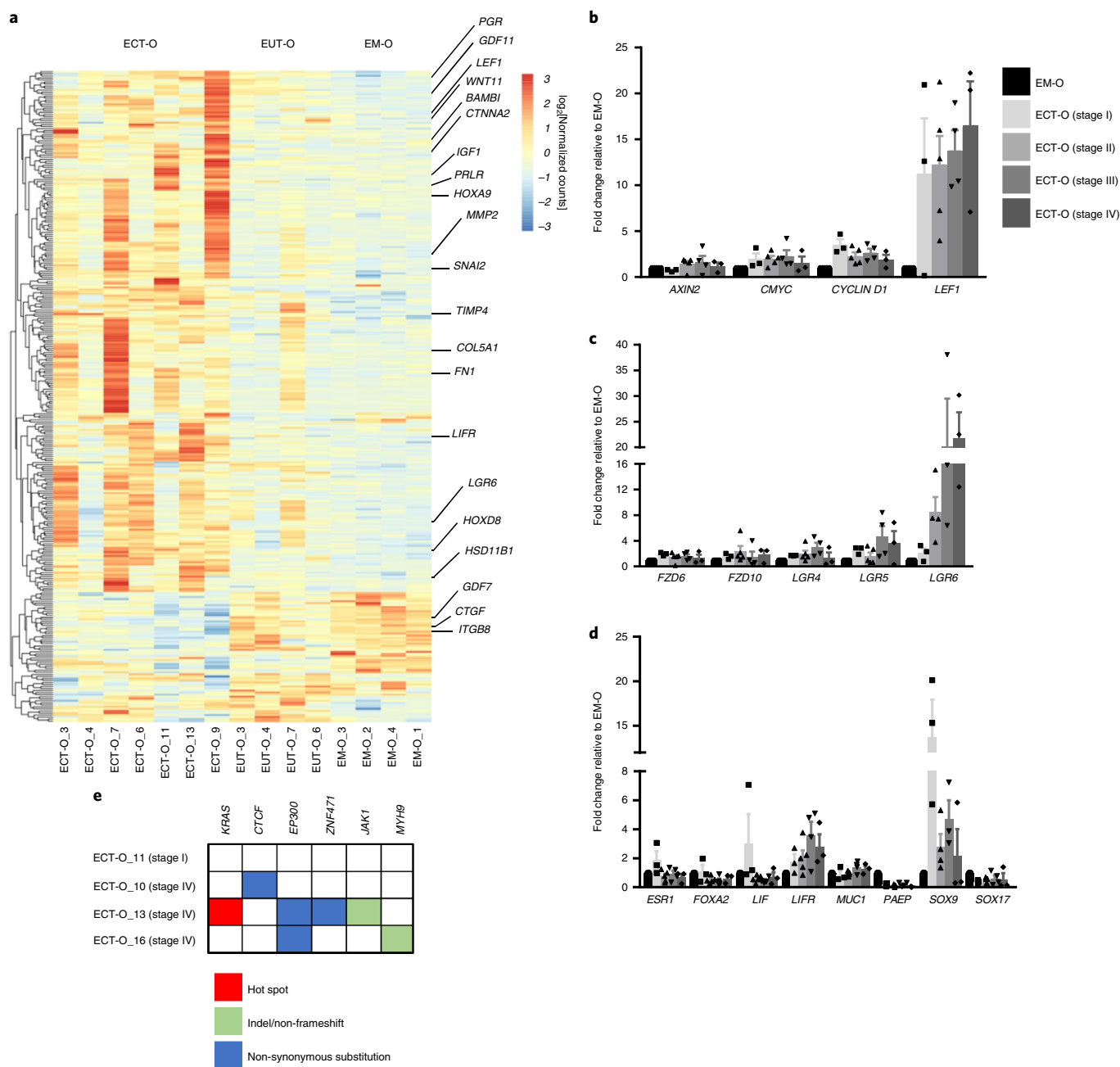


Fig. 3 | Transcriptomic analysis of ECT-O reveals disease- and stage-specific genes. **a**, A heatmap of all differentially expressed genes as identified by RNA-seq analysis of ECT-O, EUT-O and EM-O. Colours range from blue (low expression) to red (high expression). The most important genes are indicated; for the complete list, see Supplementary Tables 3–5. **b–d**, Gene expression analysis of WNT pathway targets (**b**), WNT pathway receptors (**c**) and endometrial markers (**d**) in stage I–IV ECT-O as normalized to *GAPDH* and expressed as fold change relative to EM-O (bars and error bars show the mean \pm s.e.m. of $n=3$ biologically independent experiments for stage I and stage IV ECT-O, $n=5$ for stage II ECT-O and $n=4$ for stage III ECT-O). * $P < 0.05$; non-parametric Kruskal–Wallis test for multiple comparison with Dunn's post-test. **e**, A mutation matrix representing hits in EC-associated genes as detected by WES in ECT-O. For a complete list of genetic alterations, see ArrayExpress (accession number [E-MTAB-7688](#)).

some of the lines, organoids from non-cancer endometrial cells (as present in the tumour biopsy) overtook the culture (as also reported for other cancer types^{28,29}). For instance, organoids established from a high-grade serous tumour containing multiple genomic aberrations showed a normal genome (EC-O_12; Supplementary Fig. 5c). Therefore, to make EC-O development more efficient, we assessed the influence of multiple medium components. EC-O formed better in the absence of p38i (Supplementary Fig. 5d), whereas EM-O (Fig. 1g) and HYP-O (Supplementary Fig. 5d) were negatively affected. Notably, removing p38i also improved the establishment

of other organoid types^{30,31}. Lowering p38i concentration and adding insulin-like growth factor 1 (IGF1)³², hepatocyte growth factor (HGF)³³ and lipids (which were found to be beneficial for long-term expansion; Supplementary Table 8) enhanced the establishment efficiency of EC-O (40%; Fig. 5a) and enabled their propagation for more than a year (Fig. 5b and Supplementary Fig. 5e,f). The EC-O showed prominent proliferative activity and clonogenic capacity (Fig. 5c and Supplementary Fig. 5g). We observed morphological heterogeneity between the different organoid lines (and within individual organoid cultures; Supplementary Fig. 5h). EC-O from

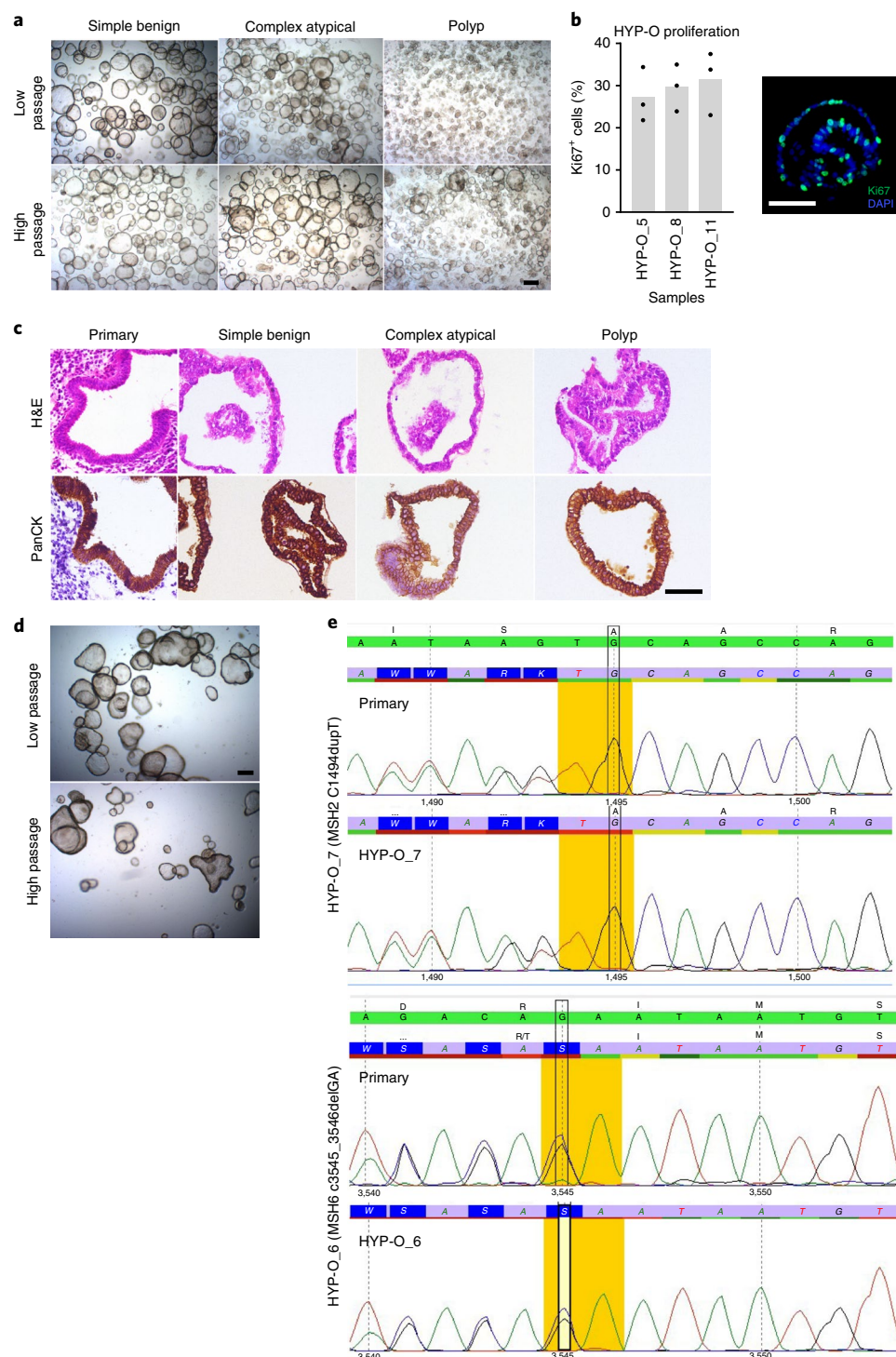


Fig. 4 | Organoids from endometrial precancer lesions display disease-associated phenotype and gene mutations. **a**, HYP-O cultures of the three main endometrial hyperplasia types at low and high passage number. Representative brightfield images of two independent donors for hyperplastic polyp and three independent donors for the other hyperplasia types are shown. Scale bar, 200 μ m. **b**, A proliferation analysis of HYP-O: the quantification of Ki67⁺ cells in organoids from three independent donors as indicated (left; bars show the mean of three technical replicates per donor) and Ki67 immunofluorescence (right; a representative image of three independent experiments (three donors); DAPI was used as the nuclear stain). Scale bar, 50 μ m. **c**, H&E analysis and PanCK immunostaining of primary hyperplastic lesions and HYP-O (simple benign, complex atypical and polyp). Representative brightfield images of two independent donors for hyperplastic polyp and three independent donors for the other hyperplasia types are shown. Scale bar, 50 μ m. **d**, Organoid cultures from endometrial biopsies of Lynch syndrome patients at low and high passage numbers. Representative brightfield images of three independent experiments (three independent donors) are shown. Scale bar, 200 μ m. **e**, Targeted sequencing results of Lynch syndrome patient endometrial biopsies (primary) and corresponding organoids. The HYP-O_7 patient harbours the heterozygote c.1494dupT (p.Ala499Cysfs*14) mutation in *MSH2* (LRG_219) as identified in the primary endometrial biopsy, which is retained in the organoids (P3); the HYP-O_6 patient harbours the heterozygote c.3545_3546delGA (p.Arg1182Asnfs*5) mutation in *MSH6* (LRG_218) as identified in the primary endometrial biopsy, which is retained in the organoids (P3).

low-grade/stage cancer generally displayed a glandular-like morphology with a well-to-moderately defined lumen (Fig. 5b,d, Supplementary Fig. 5b,h and Supplementary Video 3), whereas EC-O from high-grade/stage cancer commonly appeared dense without a visible lumen (Supplementary Fig. 5b,f,h and Supplementary Video 4). Also grade-associated degrees of nuclear abnormalities were conserved in the organoids (Supplementary Fig. 5i).

The EC-O recapitulated the (immuno)histology of the primary tumour by expressing EC-associated markers (Fig. 5d and Supplementary Fig. 5j). Expression of ER α and PR distinguishes type I from type II EC (ref. ⁶) and this was conserved in the organoids (Fig. 5d and Supplementary Fig. 5j). *PTEN* mutations depend on EC type³⁴; *PTEN* expression patterns were retained in the organoids (Supplementary Fig. 5j). Microsatellite instability (MSI) is a recurrent feature of type I EC with frequent mutations in *MLH1* and *MSH6* (ref. ³⁵). MSI phenotype was also preserved in the EC-O (Supplementary Fig. 5j). Overall, we could generate organoids from a wide variety of EC ranging from well-to-poorly differentiated types encompassing tumours with squamous (P63⁺) and mucinous (PAS⁺) differentiation (Supplementary Fig. 5j and Supplementary Table 1).

EC-O recapitulate the mutational landscape of the primary tumour and reveal disease-specific gene expression. Next, we compared the genetic make-up of primary tumours and their corresponding EC-O. First, we subjected samples to either array comparative genomic hybridization (aCGH) or low-coverage whole-genome sequencing (shallow-seq, as performed on the microsatellite-stable tumours; Supplementary Fig. 5k). These analyses revealed that the large majority of SCNA in primary tumours were retained in the corresponding EC-O, although occasional gains or losses were observed (Supplementary Fig. 5l,m).

MSI tumour types typically have stable copy number profiles but are characterized by a high mutation burden. We therefore subjected organoids derived from MSI tumours to WES (Supplementary Fig. 5k). The majority of the genetic alterations in the primary tumour were retained in the organoids even after extensive in vitro expansion (Supplementary Fig. 5n). Interestingly, a considerable number of new substitutions (1,564) were retrieved in EC-O₆ after long-term expansion (Supplementary Fig. 5n), which was not unexpected given the Lynch syndrome background. In agreement with this, EC-O₆ showed considerable SCNA after long-term expansion (Supplementary Fig. 5m).

We identified EC hotspot mutations in primary MSI tumours that were retained in the organoids even after long-term expansion (Fig. 5e). In particular, we found hotspot mutations in *FBXW7* (R465H) and *ARID1A* (R693X and R1335X) in EC-O₆ and in

PTEN (R130G) in EC-O₁₆. Furthermore, we identified genetic hits in 21 of the most frequently mutated genes in EC, in the tumour and corresponding organoids. In particular, we identified frameshift (loss-of-function) mutations in the tumour suppressor genes *PTEN*, *CTCF* and *ARID1A* and somatic mutations in *PIK3CA* (R88Q and R108H)³⁶, *TP53* (G245S)³⁶, *ARID1A*, *POLE* and *FAT1*. In addition, we found *CTNNB1* mutations in the two low-grade EC-O analysed (EC-O₂ and EC-O₃; Fig. 5e). *CTNNB1* mutations in low-grade EC lead to constitutive activity of the WNT pathway^{35,37,38}. Concordantly, we observed that low-grade EC-O showed nuclear β -catenin localization (Supplementary Fig. 5o) and higher expression of WNT target genes (for example, *AXIN2*, *LEF1*, *CMYC*, *TCF4*, *LGR6*) as compared to EM-O and high-grade EC-O (Fig. 5f and Supplementary Table 7). Accordingly, the growth of *CTNNB1*-mutant organoid lines was not affected by RSPO1 withdrawal (Fig. 5e) and less influenced by XAV939 (which inhibits WNT signalling by increasing β -catenin degradation)¹⁴ than *CTNNB1*-wild type organoid cultures (Supplementary Fig. 5o).

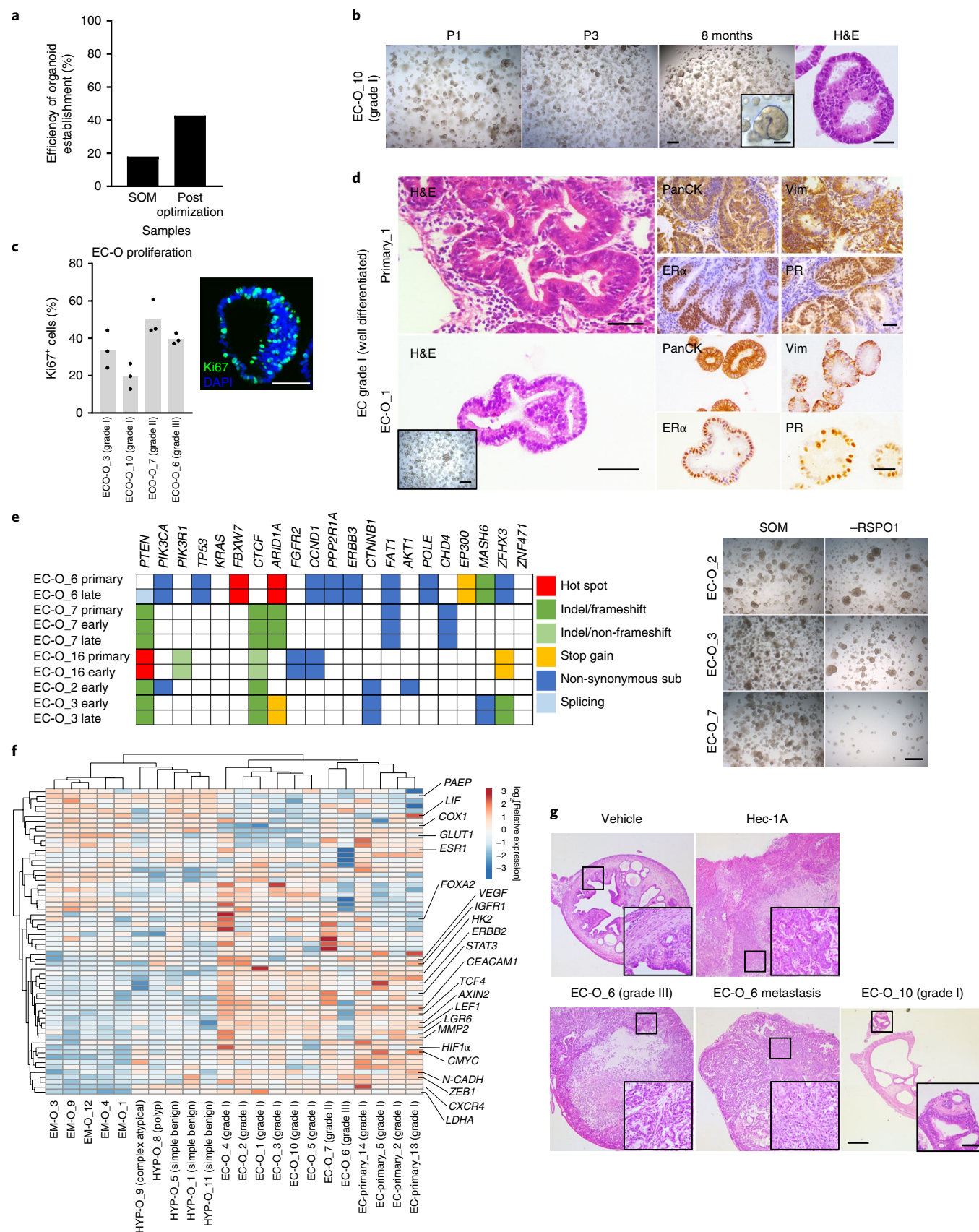
Gains in chromosome 17 are regularly observed in EC and often involve amplification of *ERBB2* (ref. ^{35,38}). We also found gains in chromosome 17 (Supplementary Fig. 5m) and observed increased *ERBB2* expression in EC-O relative to EM-O and HYP-O (Fig. 5f). We detected higher expression levels of *IGF1*, *IGFR1*, *CEACAM1* and *MMP2* in EC-O, in line with previous findings in EC (ref. ³⁸), and lower levels of endometrial markers (such as *PAEP* and *LIF*; Fig. 5f). *ESR1* and *FOXA2* were downregulated in high-grade EC-O, as reported previously in EC (ref. ³⁵; Fig. 5f). The PI3K–AKT pathway is frequently hyperactivated in EC (ref. ^{35,37}). Analogously, we found genetic alterations in the pathway's signalling mediators (*PTEN*, *PIK3CA*, *AKT1*) in several EC-O lines (Fig. 5e) as well as *STAT3*, *VEGF* and *HIF1 α* overexpression (Fig. 5f). We also detected higher expression of EMT-associated genes (*CXCR4*, *TWIST1*, *ZEB1*, *N-CADH*) in EC-O versus EM-O, while HYP-O seemed to represent an intermediate stage (Fig. 5f), as supported by clustering analysis (Supplementary Fig. 5p,q).

EC-O recapitulate disease phenotype in vivo. Subcutaneously injected EC-O generated a cell mass that replicated histological and molecular features of the primary tumour (Supplementary Fig. 6a). Following orthotopic engraftment in uterine horn, high-grade EC-O created a large, invasive, highly proliferative mass (comparable to the Hec-1A cell line) as well as peritoneal metastasis, whereas low-grade EC-O-derived lesions remained localized with lower proliferation and HYP-O generated no visible outgrowth (Fig. 5g and Supplementary Fig. 6b,c). The orthotopic grafts also reproduced the hormone receptor phenotype of the original cancer tissue (Supplementary Fig. 6c).

Fig. 5 | EC-O capture cancer heterogeneity and mutational landscape, and reveal type-associated gene expression. **a**, The efficiency of EC-O establishment before (in SOM) and after medium optimization (percentage of total biopsies seeded; $n = 22$ and 27 , respectively). **b**, Organoid cultures from low-grade (grade I) EC at low and high passage numbers (scale bar, 200 μ m; representative structure magnified in inset, scale bar, 50 μ m) and a H&E analysis (scale bar, 50 μ m). Representative brightfield images of ten biologically independent experiments are shown. **c**, A Ki67 analysis in organoids from four independent donors as indicated (left; bars show the mean of three technical replicates per donor) and Ki67 immunofluorescence (right; a representative image from four independent experiments; DAPI was used as the nuclear stain). **d**, A histological analysis of endometrial (cancer) markers in low-grade (grade I) EC and corresponding organoids (inset: a brightfield image of an organoid culture). Representative images of ten biologically independent experiments are shown. Scale bars, 50 μ m. **e**, A mutation matrix depicting hits in 21 of the most mutated genes in EC as identified by WES in primary EC samples and derived EC-O (left). Representative brightfield images of three EC-O lines harbouring *CTNNB1* mutations (or not), cultured in SOM with or without RSPO1 (right). Five independent donors were used for this experiment, each analysed in triplicate. Scale bar, 200 μ m. **f**, A heatmap of differentially expressed genes in EM-O, HYP-O, EC-O and primary tumours, as identified by RT–qPCR and presented as expression relative to *GAPDH*. Colours range from blue (low expression) to red (high expression). The most important genes are indicated; for the complete list of genes, see Supplementary Table 9. **g**, A H&E analysis of uterine horns following engraftment of EC-O or Hec-1A cells. No lesion is observed in vehicle-injected horn, which shows a preserved tissue architecture that is lost on injection of Hec-1A cells and high-grade (grade III) EC-O. The latter also gave rise to peritoneal metastasis with comparable histology. The low-grade (grade I) EC-O generated localized tumours (box). Insets: magnifications of the boxed areas. Representative images of experiments with five biologically independent donors (each in triplicate) are shown. Scale bars: 300 μ m for overviews; 50 μ m for magnifications.

EC-O show patient-specific drug responses. To explore whether EC-O are amenable to drug screening^{28–30,39}, we tested four standard chemotherapeutic compounds (paclitaxel, 5-fluorouracil,

carboplatin, doxorubicin) and everolimus (an mTOR inhibitor). The organoids showed patient-specific drug responses (Fig. 6a and Supplementary Fig. 6d). EC-O₂ was most sensitive to everolimus



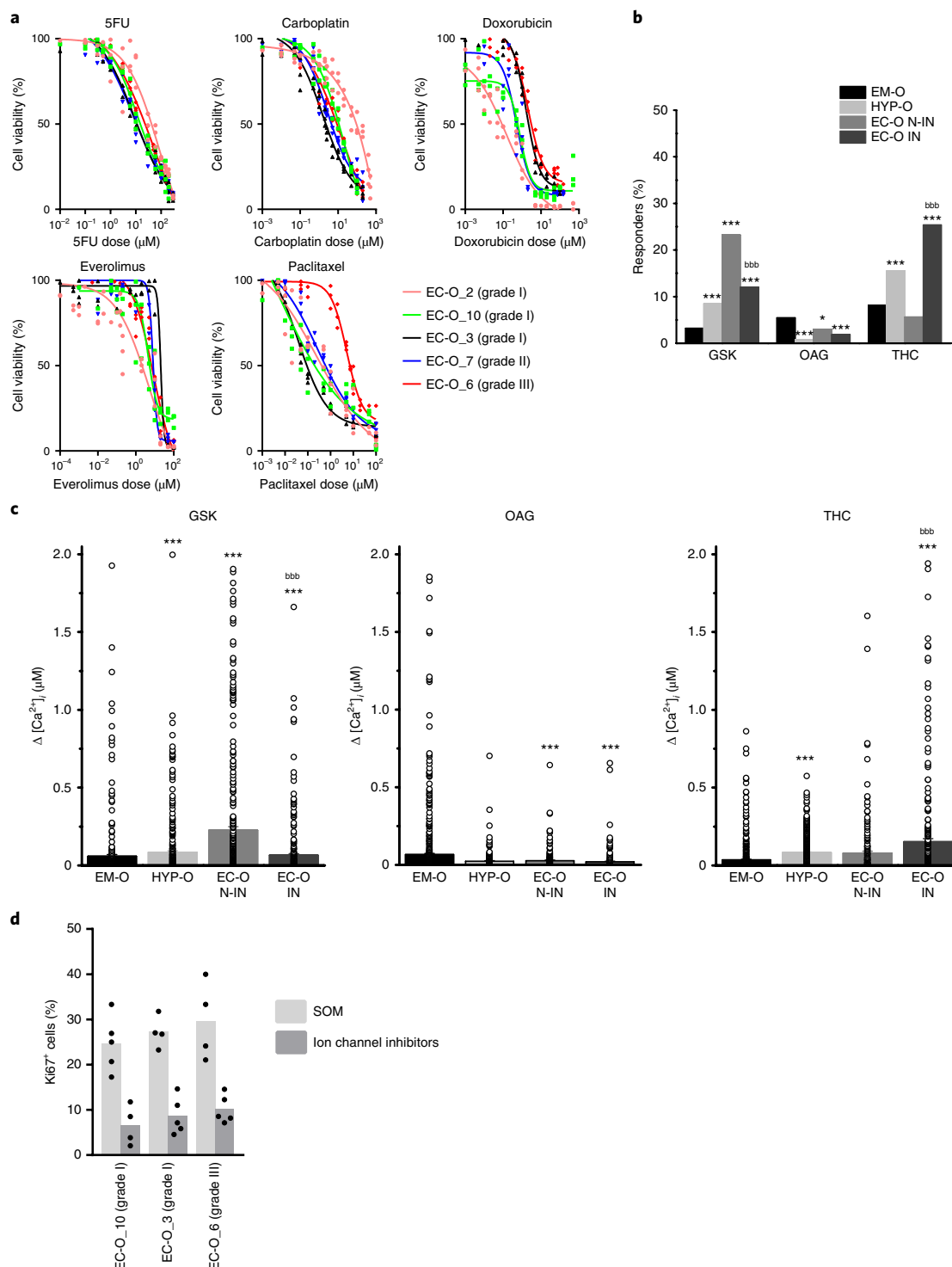


Fig. 6 | EC-O show patient-dependent drug responses and specific ion channel functionality. a, Dose–response curves of EC-O treated with the indicated drugs, as measured using the XTT cell viability assay ($n=5$ biologically independent experiments (donors); each curve represents the mean of three technical replicates per donor). The half-maximum inhibitory concentration (IC_{50}) is indicated with a dashed line for the EC-O from each individual patient (for numerical data, see Supplementary Fig. 6d). **b,** The percentage of cells that responded to specific ion channel activators in EM-O, HYP-O and EC-O, the latter subdivided into non-invasive (N-IN) and invasive (IN) phenotypes. * $P < 0.05$, *** $P < 0.001$ compared to EM-O; ^b $P < 0.001$ for EC-O IN versus EC-O N-IN; two-sided Fisher's exact test. **c,** Absolute Ca^{2+} amplitude following stimulation with the specific ion channel activator as indicated. Bars indicate the mean. *** $P < 0.001$ compared to EM-O, ^b $P < 0.001$ for EC-O IN versus EC-O N-IN; Kruskal–Wallis test with Dunn's multiple comparisons. The data in **b,c** represent the following n independent experiments encompassing the indicated total number of cells: GSK in EM-O: $n=6$, 339 cells; GSK in HYP-O: $n=6$, 363 cells; GSK in EC-O N-IN: $n=3$, 339 cells; GSK in EC-O IN: $n=2$, 357 cells; OAG in EM-O: $n=6$, 726 cells; OAG in HYP-O: $n=6$, 234 cells; OAG in EC-O N-IN: $n=3$, 224 cells; OAG in EC-O IN: $n=2$, 223 cells; THC in EM-O: $n=6$, 706 cells; THC in HYP-O: $n=6$, 485 cells; THC in EC-O N-IN: $n=3$, 195 cells; THC in EC-O IN: $n=2$, 272 cells. **d,** The percentage of Ki67^{+} cells in EC-O from three independent donors treated with a cocktail of ion channel inhibitors (or vehicle, SOM) as indicated (the bars show the mean of four or five technical replicates per donor, as represented by the individual dots).

suggesting a strong dependence on the PI3K–AKT pathway, which is in line with mutations found in the pathway's signalling mediators (*PTEN*, *PIK3CA*, *AKT1*; Fig. 5e).

Endometrial organoids show differential disease-associated expression of functional ion channels. We recently reported that EM-O conserved the functional expression of specific ion channels found in primary endometrial epithelial cells⁴⁰. To search for differences between healthy and diseased endometrium, we analysed functional ion channel expression in the organoids established here, as compared to EM-O. Regarding endometriosis, no significant differences were observed in the gene expression and functionality of the mechanosensitive channel PIEZO1 and transient receptor potential (TRP) channels (Supplementary Fig. 6e,f), in line with a recent report examining clinical biopsies⁴¹. By contrast, significant differences were found in the responses of (pre)cancerous organoids to stimulation with GSK016790A (GSK), 1-oleoyl-2-acetyl-glycerol (OAG) and Δ^9 -tetrahydrocannabinol (THC), agonists of TRPV4, TRPC6 and TRPV2, respectively (Fig. 6b and Supplementary Fig. 6g). HYP-O showed higher numbers of responding cells and increased calcium influxes (versus EM-O) in answer to GSK and THC stimulation (Fig. 6b,c). Furthermore, we found distinct responses to GSK and THC stimulation in EC-O from invasive (\geq stage IB) versus non-invasive EC, suggesting a distinct role of TRPV2 and TRPV4 in different EC stages (Fig. 6b,c). Blocking TRPV4 (together with TRPM4, TRPM7 and TRPC6) using a cocktail of available specific inhibitors strongly reduced EC-O formation efficiency in line with a decrease in proliferative activity (Fig. 6d).

Discussion

Endometrial disorders are a major gynaecological problem and cause of infertility, yet little is known about their pathogenesis. Here we developed organoids spanning a wide range of endometrial diseases. The organoids capture disease heterogeneity, maintain key features of the primary tissue, including the genetic background, and reproduce the lesion after in vivo transplantation. The organoids show strong expandability thereby overcoming the hurdle of limiting quantities of primary biopsies.

First, we established organoids from endometriotic lesions of all clinical stages that uncovered altered signalling pathways such as integrin, PI3K–AKT and WNT when compared to healthy endometrium-derived organoids. We identified EC-associated mutations in organoids from high-stage endometriosis. Together with recent reports using clinical samples^{24,25}, our findings suggest the involvement of cancer driver genes in this disease. The endometriosis organoid biobank will be valuable in deciphering disease (and type-specific) pathogenesis, especially if epithelial and stromal compartments are (re)combined in future studies^{42–44}, and in the search for drug targets that provide an alternative to current hormonal suppression therapy.

After medium optimization, long-term expandable organoids were developed from EC that captured its clinical heterogeneity. In contrast to our present study, the few endometrial tumour-derived organoid-like aggregates reported previously were not strongly characterized (essential given the risk that non-cancer organoids overtake the culture) and were not long-term expanded or in vivo grafted^{12,45,46}. We found that SCNA and the genetic landscape of tumours were largely conserved in the organoids although occasional deviations were retrieved that may be due to the genetic background of the patient, the presence of non-tumour cells in the DNA-extracted primary tissue and/or culture conditions that may favour, or hamper, the growth of specific mutant subclones (as also reported for other cancer types^{28,29}). They may also reflect the natural evolution of the cancer as occurring in vivo, as supported by the considerable number of new mutations detected in late-passage organoids from MSI Lynch syndrome tumours. EC-O show patient-

specific drug responses, thereby providing conceptual evidence that the organoids are amenable to (personalized) drug screenings. Our EC-O models provide a tool to search for pathogenetic mechanisms and drug targets.

Finally, we were also able to develop organoids from hyperplastic endometrium (including Lynch syndrome) that faithfully reproduced the disease genotype and will be valuable in the search for molecular mechanisms underlying the hyperplastic phenotype and its progression toward cancer⁴⁷.

Our study represents the start of an extended biobank (Supplementary Fig. 6h) across healthy and pathological endometrium providing promising research models and drug screening and discovery tools.

Online content

Any methods, additional references, Nature Research reporting summaries, source data, statements of code and data availability and associated accession codes are available at <https://doi.org/10.1038/s41556-019-0360-z>.

Received: 28 August 2018; Accepted: 12 June 2019;

Published online: 1 August 2019

References

- Roy, A. & Matzuk, M. M. Reproductive tract function and dysfunction in women. *Nat. Rev. Endocrinol.* **7**, 517–525 (2011).
- Deligdisch, L. Hormonal pathology of the endometrium. *Mod. Pathol.* **13**, 285–294 (2000).
- Vercellini, P., Viganò, P., Somigliana, E. & Fedele, L. Endometriosis: pathogenesis and treatment. *Nat. Rev. Endocrinol.* **10**, 261–275 (2014).
- Giudice, L. C. & Kao, L. C. Endometriosis. *Lancet* **364**, 1789–1799.
- Siegel, R. L., Miller, K. D. & Jemal, A. Cancer statistics, 2017. *CA Cancer J. Clin.* **67**, 7–30 (2017).
- Murali, R., Soslow, R. A. & Weigelt, B. Classification of endometrial carcinoma: more than two types. *Lancet Oncol.* **15**, e268–e278 (2014).
- Vollmer, G. Endometrial cancer: experimental models useful for studies on molecular aspects of endometrial cancer and carcinogenesis. *Endocr. Relat. Cancer* **10**, 23–42 (2003).
- Depreeuw, J. et al. Characterization of patient-derived tumor xenograft models of endometrial cancer for preclinical evaluation of targeted therapies. *Gynecol. Oncol.* **139**, 118–126 (2015).
- Contreras, C. M. et al. Lkb1 inactivation is sufficient to drive endometrial cancers that are aggressive yet highly responsive to mTOR inhibitor monotherapy. *Dis. Model. Mech.* **3**, 181–193 (2010).
- King, C. M., Barbara, C., Prentice, A., Brenton, J. D. & Charnock-Jones, D. S. Models of endometriosis and their utility in studying progression to ovarian clear cell carcinoma. *J. Pathol.* **238**, 185–196 (2016).
- Boretto, M. et al. Development of organoids from mouse and human endometrium showing endometrial epithelium physiology and long-term expandability. *Development* **144**, 1775–1786 (2017).
- Turco, M. Y. et al. Long-term, hormone-responsive organoid cultures of human endometrium in a chemically defined medium. *Nat. Cell Biol.* **19**, 568–577 (2017).
- American Society for Reproductive Medicine. Revised American Society for Reproductive Medicine classification of endometriosis: 1996. *Fertil. Steril.* **67**, 817–821 (1997).
- Clevers, H. & Nusse, R. Wnt/ β -catenin signaling and disease. *Cell* **149**, 1192–1205 (2012).
- Pitsos, M. & Kanakas, N. The role of matrix metalloproteinases in the pathogenesis of endometriosis. *Reprod. Sci.* **16**, 717–726 (2009).
- Eyster, K. M., Boles, A. L., Brannian, J. D. & Hansen, K. A. DNA microarray analysis of gene expression markers of endometriosis. *Fertil. Steril.* **77**, 38–42 (2002).
- Burney, R. O. et al. Gene expression analysis of endometrium reveals progesterone resistance and candidate susceptibility genes in women with endometriosis. *Endocrinology* **148**, 3814–3826 (2007).
- Matsuzaki, S. et al. DNA microarray analysis of gene expression profiles in deep endometriosis using laser capture microdissection. *Mol. Hum. Reprod.* **10**, 719–728 (2004).
- Weigel, M. T. et al. Differential expression of MMP-2, MMP-9 and PCNA in endometriosis and endometrial carcinoma. *Eur. J. Obstet. Gynecol. Reprod. Biol.* **160**, 74–78 (2012).
- Wu, Y. et al. Transcriptional characterizations of differences between eutopic and ectopic endometrium. *Endocrinology* **147**, 232–246 (2006).

21. Wu, B. et al. Reconstructing lineage hierarchies of mouse uterus epithelial development using single-cell analysis. *Stem Cell Rep.* **9**, 381–396 (2017).
22. Valentijn, A. J. et al. SSEA-1 isolates human endometrial basal glandular epithelial cells: phenotypic and functional characterization and implications in the pathogenesis of endometriosis. *Hum. Reprod.* **28**, 2695–2708 (2013).
23. Gonçalves, G. A. et al. p27^{Kip1} overexpression regulates IL-1 β in the microenvironment of stem cells and eutopic endometriosis co-cultures. *Cytokine* **89**, 229–234 (2017).
24. Anglesio, M. S. et al. Cancer-associated mutations in endometriosis without cancer. *N. Engl. J. Med.* **376**, 1835–1848 (2017).
25. Enomoto, T. et al. Clonal expansion and diversification of cancer-associated mutations in endometriosis and normal endometrium. *Cell Rep.* **24**, 1777–1789 (2018).
26. Jeong, J.-W. et al. beta-catenin mediates glandular formation and dysregulation of beta-catenin induces hyperplasia formation in the murine uterus. *Oncogene* **28**, 31–40 (2009).
27. Lynch, H. T., Snyder, C. L., Shaw, T. G., Heinen, C. D. & Hitchins, M. P. Milestones of Lynch syndrome: 1895–2015. *Nat. Rev. Cancer* **15**, 181–194 (2015).
28. Broutier, L. et al. Human primary liver cancer-derived organoid cultures for disease modeling and drug screening. *Nat. Med.* **23**, 1424–1435 (2017).
29. Gao, D. et al. Organoid cultures derived from patients with advanced prostate cancer. *Cell* **159**, 176–187 (2014).
30. Sachs, N. et al. A living biobank of breast cancer organoids captures disease heterogeneity. *Cell* **172**, 373–386 (2018).
31. Fujii, M. et al. Human intestinal organoids maintain self-renewal capacity and cellular diversity in niche-inspired culture condition. *Cell Stem Cell* **23**, 787–793 (2018).
32. Aizen, D. et al. Proliferative and signaling activities of insulin analogues in endometrial cancer cells. *Mol. Cell. Endocrinol.* **406**, 27–39 (2015).
33. Yoshida, S. et al. Induction of hepatocyte growth factor in stromal cells by tumor-derived basic fibroblast growth factor enhances growth and invasion of endometrial cancer. *J. Clin. Endocrinol. Metab.* **87**, 2376–2383 (2002).
34. Risinger, J. I. et al. PTEN mutation in endometrial cancers is associated with favorable clinical and pathologic characteristics. *Clin. Cancer Res.* **4**, 3005–3010 (1998).
35. Getz, G. et al. Integrated genomic characterization of endometrial carcinoma. *Nature* **497**, 67–73 (2013).
36. McConechy, M. K. et al. Use of mutation profiles to refine the classification of endometrial carcinomas. *J. Pathol.* **228**, 20–30 (2012).
37. Yeramian, A. et al. Endometrial carcinoma: molecular alterations involved in tumor development and progression. *Oncogene* **32**, 403–413 (2013).
38. Salvesen, H. B. et al. Integrated genomic profiling of endometrial carcinoma associates aggressive tumors with indicators of PI3 kinase activation. *Proc. Natl Acad. Sci. USA* **106**, 4834–4839 (2009).
39. Van De Wetering, M. et al. Prospective derivation of a living organoid biobank of colorectal cancer patients. *Cell* **161**, 933–945 (2015).
40. Hennes, A. et al. Functional expression of the mechanosensitive PIEZO1 channel in primary endometrial epithelial cells and endometrial organoids. *Sci. Rep.* **9**, 1779 (2019).
41. Persoons, E. et al. Functional expression of TRP ion channels in endometrial stromal cells of endometriosis patients. *Int. J. Mol. Sci.* **19**, 2467 (2018).
42. Seino, T. et al. Human pancreatic tumor organoids reveal loss of stem cell niche factor dependence during disease progression. *Cell Stem Cell* **22**, 454–467 (2018).
43. Stzepourginski, I. et al. CD34+ mesenchymal cells are a major component of the intestinal stem cells niche at homeostasis and after injury. *Proc. Natl. Acad. Sci. USA* **114**, E506–E513 (2017).
44. Öhlund, D. et al. Distinct populations of inflammatory fibroblasts and myofibroblasts in pancreatic cancer. *J. Exp. Med.* **214**, 579–596 (2017).
45. Pauli, C. et al. Personalized in vitro and in vivo cancer models to guide precision medicine. *Cancer Discov.* **7**, 462–477 (2017).
46. Girda, E., Huang, E. C., Leiserowitz, G. S. & Smith, L. H. The use of endometrial cancer patient-derived organoid culture for drug sensitivity testing is feasible. *Int. J. Gynecol. Cancer* **27**, 1701–1707 (2017).
47. Drost, J. et al. Use of CRISPR-modified human stem cell organoids to study the origin of mutational signatures in cancer. *Science* **358**, 234–238 (2017).

Acknowledgements

We thank our other colleagues (H.V. group: Y. Van Goethem; Stem Cell Institute: A. Santo Ramalho Venâncio; D. Costamagna; P. Peetermans) for their valuable input and technical help. We are also grateful to J. Laureys (Department of Clinical and Experimental Medicine, KU Leuven) and K. Eggermont for their expert help in mouse transplantation experiments, and to the patients, staff and nurses at UZ Leuven for providing the clinical samples. We thank the VIB Nucleomics Core and KU Leuven Genomics Core (particularly Á. Calabuig) for their expert assistance in RNA-seq and aCGH analysis. We are also grateful to InfraMouse (VIB–KU Leuven, Hercules type 3 project ZW09-03) for the use of histological instruments and microscopes. Finally, we acknowledge the use of the Electron Microscopy Platform of the Centre for Human Genetics (VIB–KU Leuven). This work was supported by grants from the KU Leuven Research Fund and from the FWO–Flanders (Belgium). A.H., I.V.Z. and B.C. are supported by a PhD Fellowship from the FWO. M.B. is a PhD Fellow supported by a GOA grant from the Research Fund of the KU Leuven. D.T. is a Senior Clinical Investigator of the FWO.

Author contributions

M.B. designed the concepts and experiments, performed the experiments and the data analysis and interpreted the results. M.B. and H.V. wrote the manuscript. N.M. contributed to the EC-O protocol set-up, drug screenings, gene expression analyses and routine organoid culturing. X.L. provided essential help in the bioinformatic analysis of RNA-seq data. A.H. performed and cointerpreted the functional ion channel analysis. B.Bo. performed the genomic screening. B.Bo. and D.L. cointerpreted the genomic screening. D.L. supervised the genomic screening. B.Bu., L.P., R.H. and B.C. helped to maintain the organoid cultures. B.Bu. and L.P. helped to perform gene expression analyses. R.H. collected patient information and samples and helped to perform the molecular analyses. H.K. performed and cointerpreted the TEM. I.V.Z. recorded the 3D organoid videos. H.B. guided and supervised the targeted sequencing analysis. M.F. and T.D. added conceptual input. M.F. provided culture essentials. H.U. supervised the 3D imaging. K.P.K. supervised the bioinformatic analyses. A.V., C.M., C.T. and D.T. were driving forces in setting up the clinical collaboration to obtain human samples. I.V. was a collaborating surgeon who provided many of the clinical samples. C.M. and C.T. performed the laparoscopy. C.M., C.T. and D.T. are collaborating gynaecologists with joint grant applications in endometrial research. J.V. supervised and cointerpreted the functional ion channel analysis and is a collaborating scientist with joint grant applications in endometrial research. D.T. performed surgery. H.V. designed and supervised the project, codeveloped the concepts and ideas, codesigned the experiments and coanalysed and cointerpreted the data. All coauthors critically read and approved the manuscript.

Competing interests

The authors declare no competing interests.

Additional information

Supplementary information is available for this paper at <https://doi.org/10.1038/s41556-019-0360-z>.

Reprints and permissions information is available at www.nature.com/reprints.

Correspondence and requests for materials should be addressed to M.B. or H.V.

Publisher's note: Springer Nature remains neutral with regard to jurisdictional claims in published maps and institutional affiliations.

© The Author(s), under exclusive licence to Springer Nature Limited 2019

Methods

Organoid culturing from endometrial and endometriotic biopsies. Biopsies were obtained from patients with different endometrial conditions (see Supplementary Table 1) after informed written consent. The study was approved by the Ethical Research Committee UZ/KU Leuven (S59006; S59177) and is compliant with all relevant ethical regulations regarding research involving human participants. Biopsies were minced into small pieces and extensively rinsed in $\text{Ca}^{2+}/\text{Mg}^{2+}$ -free PBS (10010023, Thermo Fisher Scientific). Tissue samples were dissociated using collagenase IV ($1\text{--}2\text{ mg ml}^{-1}$; 17104019, Thermo Fisher Scientific) in the presence of Rock inhibitor (RI; Y-27632, $10\text{ }\mu\text{M}$; SCM075, Merck Millipore) and mechanical trituration for 1–3 h. Subsequently, tissue was incubated for 15 min in TrypLE ($1\times$; 12604013, Thermo Fisher Scientific) supplemented with RI. Digestion was stopped by medium dilution (without serum) and, after centrifugation, the pellet was resuspended in 70% Matrigel/30% DMEM/F12 (356231, Corning and 11330032, Thermo Fisher Scientific, respectively) supplemented with RI, and 20- μl droplets were deposited in prewarmed 48-well plates. Organoids were cultured as previously described¹¹ with minor medium modifications (Supplementary Table 2). For passaging (performed every 10–20 d), organoids were recovered by liquifying the Matrigel drop with ice-cold DMEM/F12 (without any enzymes, growth factors or serum) and mechanical pipetting to ensure the maximum collection of organoids. Subsequently, the organoids were dissociated using TrypLE (in DMEM/F12 containing RI) and mechanically triturated; the mixture was centrifuged at 230g. The fragments and cells obtained were resuspended in 70% Matrigel/30% DMEM/F12 supplemented with RI and droplets were deposited in 48-well plates. Established organoids were amplified, cryopreserved for biobanking and subjected to downstream analyses (Supplementary Fig. 1a). Unless otherwise stated, organoids of low passage number (P3–P6) were used for the experiments described.

To assess clonogenic capacity, organoids were dissociated into single cells with TrypLE supplemented with RI, filtered through a 40- μm cell strainer and resuspended in 70% Matrigel/30% DMEM/F12 supplemented with RI at 10–100 cells per well. The organoids formed were counted after 20–30 d.

Testing medium compounds and the rescue of IWP2 effect in organoid culturing.

Organoids were cultured for at least three passages in SOM (Supplementary Table 2), then dissociated with TrypLE supplemented with RI and seeded in 70% Matrigel/30% DMEM/F12 supplemented with RI at 1,000 cells per well in 96-well plates. Cells were cultured in SOM from which individual compounds were omitted. The number of sizeable organoids ($>300\text{ }\mu\text{m}$) formed was determined after 7–20 d and averaged for three independent patient donors.

Dissociated organoid cells (from five independent donors) were seeded as described above and cultured for ten consecutive days in SOM (without RSP01 and IWP2 ($1\text{ }\mu\text{M}$; 10536–5MG, Sigma Aldrich), to which RSP01 (Supplementary Table 2), WNT3A (200 ng ml^{-1} ; 5036–WN-010, R&D systems), WNT5A (500 ng ml^{-1} ; 645–WN-010, R&D systems) or WNT7A ($1\text{ }\mu\text{g ml}^{-1}$; 3008–WN-025, R&D systems) were added. The medium was refreshed every 2 d and the number of organoids counted after 10 d. To assess the expression of downstream target genes, mature organoids were cultured for 72 h in the specified conditions and extracted RNA was subjected to RT–qPCR as described below. In some experiments, XAV939 (10 nM ; 3748, Tocris Bioscience) was used as a WNT pathway inhibitor.

In vivo transplantation. Organoids that had been expanded for four to six passages were removed from the Matrigel, trypsinized and resuspended in 50 μl of PBS for transplantation under the kidney capsule or in 200 μl for intraperitoneal injection. For subcutaneous transplantation, organoids were resuspended in 200 μl of 50% Matrigel/50% PBS. These transplantation experiments were performed in ovariectomized NOD–SCID mice in which an oestradiol pellet was subcutaneously implanted at the time of ovariectomy (as previously described¹¹). For uterine injection, organoids were resuspended in 20 μl of 100% Matrigel and injected into the exposed uterine horn of anaesthetized NOD–SCID mice. The EC cell line Hec-1A (used as a positive control) was obtained from ATCC (LGC Standards) and cultured in DMEM/F12 with 10% fetal bovine serum (12103C, Sigma Aldrich). Mouse experiments were approved by the KU Leuven Ethical Committee for Experimental Animals and performed in compliance with all ethical regulations regarding animal research. After the indicated period of time, mice were killed, grafts (and potential metastasis) localized and tissues processed for (immuno)histological analysis.

Immunohistochemical analysis. Examinations were performed as previously described¹¹. In brief, paraffin sections were subjected to antigen retrieval and incubated overnight with primary antibody (Supplementary Table 10) and subsequently with horseradish peroxidase-conjugated secondary antibody (ImmPRESS horseradish peroxidase universal antibody peroxidase-conjugated horse antimouse IgG/anti-rabbit IgG polymer detection kit; MP-7500, Vector Laboratories). Sections were counterstained with haematoxylin. PAS staining was performed to visualize the mucin according to the manufacturer's instructions (395B-1KT, Sigma Aldrich)¹¹.

TEM. TEM analysis was performed as previously described in detail¹¹. In brief, organoids were removed from the Matrigel and sequentially fixed in

glutaraldehyde and osmium tetroxide/potassium ferrocyanide. Organoids were incubated with tannic acid (403040, Sigma Aldrich) for 20 min and uranyl acetate (AGRI260A, Agar Scientific) overnight, followed by aspartate (A9256, Sigma Aldrich) for 30 min. Samples were dehydrated and embedded in epoxy resin (Agar 100; AGR1031, Agar Scientific) and 70 nm sections were analysed using a JEM1400 transmission electron microscope (JEOL) equipped with an Olympus SIS Quemesa 11 megapixel camera.

Two-photon excitation microscopy. Organoids were fixed with 4% paraformaldehyde for 30 min at 37 °C, washed with PBS and incubated with Hoechst 33342 ($2.5\text{ }\mu\text{g ml}^{-1}$ in PBS; H6024, Sigma Aldrich) for 1 h at 37 °C. After rinsing, Vybrant DiI cell-labelling solution ($0.1\text{ }\mu\text{M}$ in PBS; V2288, Thermo Fisher Scientific) was applied and organoids incubated for 2 h. z-stacks (up to 350 μm) were acquired with a confocal microscope (Leica TCS SP8 X) equipped with a Mai Tai DeepSee multiphoton laser (Spectra physics) and a $\times 40$ long-working distance objective (HC PL IRAPO $\times 40/1.10\text{ W CORR}$). Emission light was detected with Hybrid Refractive light Detectors (HyD RLD, Leica).

aCGH. Organoids were recovered from the Matrigel; genomic DNA from the organoids and primary tissues was isolated using the Purelink Genomic Mini Kit (K182001, Invitrogen) according to the manufacturer's instructions. aCGH analysis was performed using the 8 \times 60 k CytoSure ISCA v3 microarray (Oxford Gene Technology). Genomic DNA was labelled for 2 h with the CytoSure Labelling Kit (020020, Oxford Gene Technology). Samples were labelled with Cy5 and hybridized to Cy3-labelled sex-matched reference DNA. Hybridization was performed for at least 16 h at 65 °C in a rotator oven (SciGene). Arrays were rinsed using Agilent wash solutions with a Little Dipper Microarray Processor (SciGene) and scanned using an Agilent microarray scanner at 2 μm resolution, followed by the calculation of signal intensities using Feature Extraction software (Agilent Technologies). Result visualization and data analysis were performed using CytoSure Interpret Software and a circular binary segmentation algorithm. Quality control metrics were monitored with CytoSure Interpret software.

Targeted sequencing. Genomic DNA was amplified using targeted primers (sequences are available on request) and sequenced bidirectionally using ABI BigDye Terminator Sequencing 3.1 on the ABI3730XL instrument (Thermo Fisher Scientific). Nucleotide numbering reflects the cDNA transcript with +1 corresponding to the A of the ATG translation initiation codon in the reference sequence for *MSH2* (LRG_218) and *MSH6* (LRG_219).

Library preparation and genomic screening. The genomic screen was performed according to the flowchart depicted in Supplementary Fig. 5k. Whole-genome DNA libraries were created using the Illumina TruSeq DNA sample preparation kit V2 (FC-121, Illumina) according to the manufacturer's instructions. The exome was captured with the Nimblegen SeqCap EZ Developer Library kit and TP53 and MSI libraries created by amplicon-based enrichment. All resulting libraries were sequenced on HiSeq4000 (Illumina) using a V3 flowcell generating 2 \times 151 base pair reads.

Raw sequencing reads of whole-exome libraries were mapped to the human reference genome (GRCh37/hg19) using Burrows–Wheeler Aligner⁴⁸. Samples were sequenced with an average sequencing depth of 23 \times and 85% of the exome was covered over 10 \times . PCR duplicates (on average 15%) were removed with Picard (v1.43). Genome Analysis Toolkit 2 (GATK; ref. ⁴⁹) was applied to perform base recalibration and local realignment around indels. Substitutions were called by GATK, whereas small indels were detected using Dindel (v1.01; ref. ⁵⁰). Only substitutions with a quality score >30 and indels with a quality score >50 and a minimum of 10 reads, and a tumour allelic frequency of 10% for both, were considered. To limit the detection of SNPs, mutations were further filtered by removing the common mutations present in the ESP6500v2, the 1,000 Genomes Project 2015, the Complete Genomics 46 and the Exome Aggregations Consortium databases, as well as the Genome of the Netherlands and a database consisting of 100 germ-line samples previously sequenced in our lab. The remaining mutations were annotated using ANNOVAR⁵¹. Raw sequencing reads of the TP53 libraries were analysed in a similar manner using a target interval limited to the TP53 region to reduce computational effort, while the MSI status was assessed as previously described⁵².

Raw sequencing reads from whole-genome libraries were mapped to GRCh37/hg19, duplicates removed and reads further analysed by QDNAseq (ref. ⁵⁰) resulting in read counts per bin of 50 kilobases. The Ascat algorithm was used for the segmentation of these data.

RNA-seq. RNA was extracted from organoids with the RNeasy Mini Kit (74104, Qiagen) according to the manufacturer's instructions. RNA quality was analysed using Agilent picochips on an Agilent BioAnalyzer 2100. Only samples with RNA integrity number (RIN) ≥ 7.5 were subjected to RNA-seq. RNA was amplified with the Smart-Seq V4 kit (634894, Takara Bio Europe) and libraries were prepared using the NEBNext Ultra DNA Library prep kit (E7370S, Illumina), followed by sequencing on NextSeq500 (Illumina). The index trimmed single-end 75 base pair reads were aligned to the human reference genome (hg38) using Hisat2 (v2.1.0)

to generate bam files. The gene-level read count matrix was summarized from bam files using featureCounts (v1.5.3). The count matrix was imported into the R Bioconductor DESeq2 package (v1.18.1) for differential gene expression analysis with a false discovery rate < 0.1. The differentially expressed genes obtained were then used to generate heatmaps by applying R package pheatmap (v1.0.8; <https://cran.r-project.org/web/packages/pheatmap/>) with scaling and clustering of only the rows. PCA was performed using the plotPCA function from the DESeq2 package with unsupervised transformed counts. Gene ontology analysis was performed using Gene Ontology Consortium software (<http://geneontology.org/>) and DAVID (<https://david.ncifcrf.gov/>) while pathway analysis was performed using the KEGG PATHWAY Database (<https://www.genome.jp/kegg/pathway.html>).

SNP variant calling of RNA-seq data. Raw reads in fastq format were filtered for adapters with ea-utils fastq-mcf (v1.1.2). Adapter-free reads were aligned to the human reference genome (hg19; Ensemble version 75) using the splice-aware package Tophat2 (ref. 53). Resulting bam files were merged per lane with Samtools (v1.5). RNA-seq variant calling was performed following GATK best practices on a GATK 3.6 haplotype caller⁴⁸. Resulting VCF files were merged with vcftools and indexed with tabix. Variant annotation was performed with ANNOVAR (ref. 4; against hg19).

Gene expression analysis by RT-qPCR. RNA was reverse-transcribed and subjected to SYBR Green- or TaqMan assay-based real-time qPCR as previously described^{11,54}, using forward and reverse primers as presented in Supplementary Table 11. *GAPDH*, *HPRT1* and/or *PGK1* were used as housekeeping genes (HKG). Relative gene expression levels were calculated as ΔC_t values ($C_{t_{\text{gene}}} - C_{t_{\text{HKG}}}$) and presented as $\log[2^{-(C_{t_{\text{gene}}} - C_{t_{\text{HKG}}})} \times 1,000]$ or as fold change compared to EM-O (reference) using the formula $2^{-(\Delta C_{t_{\text{sample}}} - \Delta C_{t_{\text{reference}}})}$. Bar graphs were generated with GraphPad Prism (Version 7.03) while heatmaps were produced with ClustVis (web tool for visualizing the clustering of multivariate data; BETA).

Drug screening. Tumour organoids were recovered from the Matrigel and dissociated. 2,000 cells were seeded in 96-well plates and allowed to form organoids for 10 d. Then, paclitaxel (Paclitaxel AB; T7402, Aurobindo), 5-fluorouracil (Fluracedyl; 3385, Teva), carboplatin (2626, Tocris), doxorubicin (D1515-10MG, Sigma Aldrich) or everolimus (6188, Tocris) were added at various concentrations and viability was measured after 72 h using the XTT assay (X6493, Invitrogen) following the manufacturer's instructions. The vehicle (DMSO; D8418, Sigma Aldrich) was used as a negative control. Dose-response curves and IC_{50} values were calculated using Graphpad Prism (Version 7.03).

Ion channel functionality. Analysis of ion channel functionality was performed by calcium microfluorimetry as previously described in detail⁴⁰. Briefly, dissociated organoid cells were seeded on collagen-coated coverslips in a 12-well plate, incubated with Fura-2 acetoxymethyl ester (2 μ M; F1201, Thermo Fisher Scientific) and intracellular Ca^{2+} was measured after exposure to specific ion channel activators, that is THC (50 μ M; kindly provided by G. Appendino, Università del Piemonte Orientale) for TRPV2, GSK (10 nM; G0798, Sigma Aldrich) for TRPV4 and OAG (100 μ M; 495414, Calbiochem) for TRPC6. Absolute Ca^{2+} concentrations and amplitudes were calculated and responding cells identified. Only cells that responded to the positive control ionomycin (2 μ M; I24222, Thermo Fisher Scientific) at the end of the experiment were taken into account.

To block ion channel activity, we added a cocktail of available specific inhibitors, that is flufenamic acid (10 μ M; F9005, Sigma Aldrich), NS8593 (30 μ M; 4597, Tocris), HC067047 (100 μ M; SML0143, Sigma Aldrich) and larixyl

acetate (2 μ M; 2730595, Sigma Aldrich), blocking TRPM4, TRPM7, TRPV4 and TRPC6, respectively. Analysis of the impact on organoid (EC-O) formation and proliferation (Ki67 immunostaining) was performed 72 h later.

Statistical analyses and reproducibility. Normal distribution was verified before performing statistical analyses. In the case of normal distribution, multiple comparisons were analysed using one- or two-way ANOVA followed by Dunnett's test for multiple comparison (95% confidence intervals). When normal distribution was not achieved, multiple comparisons were analysed using a non-parametric Kruskal-Wallis test with Dunn's post-test (95% confidence intervals). Statistical significance was defined as $P < 0.05$. All statistical analyses were calculated using GraphPad Prism (Version 7.03). All experiments were performed with at least three independent biological experiments (patient donors) per group and each experiment had three technical replicates. Multiple operators performed the experiments and similar results were obtained. For figures where representative images are shown, the number of times that the experiment was repeated independently with similar results is mentioned in the legend.

Reporting Summary. Further information on research design is available in the Nature Research Reporting Summary linked to this article.

Data availability

RNA-seq data were deposited in the Gene Expression Omnibus with accession number GSE118928. Raw sequencing reads of shallow-seq and WES have been deposited in the ArrayExpress database at EMBL-EBI (www.ebi.ac.uk/arrayexpress) under accession numbers E-MTAB-7687 and E-MTAB-7688, respectively. Source data for Fig. 1b-d, Fig. 3b-d, Fig. 4b, Fig. 5a-c, Fig. 6a-d, Supplementary Fig. 1d-g-i, Supplementary Fig. 2b, Supplementary Fig. 3c-d, Supplementary Fig. 5d,e,g and Supplementary Fig. 6d-g reported in this study are provided as supplementary source data tables in Supplementary Table 12. All other data supporting the findings of this study are available from the corresponding authors on reasonable request. Unique biological materials can be made available to third parties depending on their research goals (that is, an absence of a conflict of interest), mutual ethical permissions and a Material Transfer Agreement.

References

- Li, H. & Durbin, R. Fast and accurate short read alignment with Burrows-Wheeler transform. *Bioinformatics* **25**, 1754-1760 (2009).
- Van der Auwera, G. A. et al. From FastQ files to high confidence variant calls: the genome analysis toolkit best practices pipeline. *Curr. Protoc. Bioinform.* **43**, 1-33 (2013).
- Albers, C. A. et al. Dindel: accurate indel calls from short-read data. *Genome Res.* **21**, 961-973 (2011).
- Wang, K., Li, M. & Hakonarson, H. ANNOVAR: functional annotation of genetic variants from high-throughput sequencing data. *Nucleic Acids Res.* **38**, e164 (2010).
- Zhao, H. et al. Mismatch repair deficiency endows tumors with a unique mutation signature and sensitivity to DNA double-strand breaks. *eLife* **3**, (2014).
- Kim, D. et al. TopHat2: accurate alignment of transcriptomes in the presence of insertions, deletions and gene fusions. *Genome Biol.* **14**, R36 (2013).
- De Clercq, K. et al. The functional expression of transient receptor potential channels in the mouse endometrium. *Hum. Reprod.* **32**, 615-630 (2017).

Reporting Summary

Nature Research wishes to improve the reproducibility of the work that we publish. This form provides structure for consistency and transparency in reporting. For further information on Nature Research policies, see [Authors & Referees](#) and the [Editorial Policy Checklist](#).

Statistics

For all statistical analyses, confirm that the following items are present in the figure legend, table legend, main text, or Methods section.

n/a Confirmed

- ☐ ☒ The exact sample size (n) for each experimental group/condition, given as a discrete number and unit of measurement
- ☐ ☒ A statement on whether measurements were taken from distinct samples or whether the same sample was measured repeatedly
- ☐ ☒ The statistical test(s) used AND whether they are one- or two-sided
Only common tests should be described solely by name; describe more complex techniques in the Methods section.
- ☒ ☐ A description of all covariates tested
- ☐ ☒ A description of any assumptions or corrections, such as tests of normality and adjustment for multiple comparisons
- ☐ ☒ A full description of the statistical parameters including central tendency (e.g. means) or other basic estimates (e.g. regression coefficient) AND variation (e.g. standard deviation) or associated estimates of uncertainty (e.g. confidence intervals)
- ☐ ☒ For null hypothesis testing, the test statistic (e.g. F , t , r) with confidence intervals, effect sizes, degrees of freedom and P value noted
Give P values as exact values whenever suitable.
- ☒ ☐ For Bayesian analysis, information on the choice of priors and Markov chain Monte Carlo settings
- ☒ ☐ For hierarchical and complex designs, identification of the appropriate level for tests and full reporting of outcomes
- ☒ ☐ Estimates of effect sizes (e.g. Cohen's d , Pearson's r), indicating how they were calculated

Our web collection on [statistics for biologists](#) contains articles on many of the points above.

Software and code

Policy information about [availability of computer code](#)

Data collection

TEM was analyzed using a JEM1400 transmission electron microscope (JEOL) equipped with an Olympus SIS Quemesa 11Mpxl camera. For array CGH, arrays were scanned using an Agilent microarray scanner followed by calculation of signal intensities using Feature Extraction software (Agilent Technologies). The information on how the data were obtained is indicated in the Methods section of the manuscript.

Data analysis

For the RNA sequencing analysis, the index trimmed single-end 75bp reads were aligned to the human reference genome (hg38) using Hisat2 (v2.1.0) to generate bam files. Gene-level read count matrix was summarized from bam files using featureCounts (v1.5.3). The count matrix was imported into the R Bioconductor DESeq2 package (v1.18.1) for differential gene expression analysis with false discovery rate (FDR) <0.1. The differentially expressed genes obtained were then used to generate heatmaps by applying R package pheatmap (v1.0.8; <https://cran.r-project.org/web/packages/pheatmap/>) with scaling and clustering of only the rows. PCA was performed using plotPCA function from DESeq2 package with unsupervised transformed counts. Gene ontology (GO) analysis was done using Gene Ontology Consortium software (<http://geneontology.org/>) and DAVID (<https://david.ncifcrf.gov/>) while pathway analysis was performed using the KEGG PATHWAY Database (<https://www.genome.jp/kegg/pathway.html>). For gene expression analysis, bar graphs were generated with GraphPad Prism (Version 7.03) while heatmaps were produced with ClustVis (web tool for visualizing clustering of multivariate data; BETA). All statistical analyses were performed with GraphPad Prism (Version 7.03). For array CGH, result visualization and data analysis were performed using CytoSure Interpret Software and circular binary segmentation algorithm. For the histochemical analyses, images were analyzed with imageJ (version 2006.02.01). For the WES analysis, raw sequencing reads of whole-exome libraries were mapped to the human reference genome (GRCh37/hg19) using Burrows-Wheeler Aligner. Samples were sequenced with average sequencing depth of 23x and 85% of the exome was covered over 10x. PCR duplicates (on average 15%) were removed with Picard (v1.43). Genome Analysis Toolkit 2 (GATK) was applied to perform base recalibration and local realignment around indels. Substitutions were called by GATK, whereas small indels were detected using Dindel (v1.01). Only substitutions with a quality score >Q30 and indels with a quality score >50 and a minimum of 10 reads, and tumor allelic frequency of 10% for both, were considered. To limit the detection of SNPs, mutations were further filtered by removing the common mutations present in the ESP6500v2, the 1000 genome project 2015, the complete genomics 46 and the ExAC (Exome Aggregations Consortium) databases, as well as the Genome of the Netherlands and a database consisting of 100 germ-line samples earlier sequenced in our lab. The remaining mutations were annotated using ANNOVAR.

Raw sequencing reads of the TP53 libraries were analyzed in a similar manner using a target interval limited to the TP53 region to reduce computational effort, while the MSI status was assessed as previously described. Raw sequencing reads from whole-genome libraries were mapped to GRCh37/hg19, duplicates removed, and reads further analyzed by QDNAseq resulting in read counts per bin of 50kb. Ascat algorithm was used for segmentation of these data. For SNP variant calling of RNA-seq data, raw reads in fastq format were filtered for adapters with ea-utils fastq-mcf (v1.1.2). Adapter-free reads were aligned to the human reference genome (hg19; Ensemble version 75) using the splice-aware package Tophat 2. Resulting BAM files were merged per lane with Samtools (v1.5). RNA-seq variant calling was performed following the GATK's best practices on GATK 3.6 haplotype caller. Resulting VCF files were merged with vcf-tools and indexed with tabix. Variant annotation was performed with ANNOVAR (against hg19). All this information has been provided in the Methods section of the manuscript.

For manuscripts utilizing custom algorithms or software that are central to the research but not yet described in published literature, software must be made available to editors/reviewers. We strongly encourage code deposition in a community repository (e.g. GitHub). See the Nature Research [guidelines for submitting code & software](#) for further information.

Data

Policy information about [availability of data](#)

All manuscripts must include a [data availability statement](#). This statement should provide the following information, where applicable:

- Accession codes, unique identifiers, or web links for publicly available datasets
- A list of figures that have associated raw data
- A description of any restrictions on data availability

RNA-seq data have been deposited in Gene Expression Omnibus (GEO) with accession number GSE118928. Raw sequencing reads of shallow-seq and WES have been deposited in the ArrayExpress database at EMBL-EBI (www.ebi.ac.uk/arrayexpress) under accession number E-MTAB-7687 and E-MTAB-7688, respectively. Source data for Fig. 1b-d,g, Fig. 3b-d, Fig. 4b, Fig. 5a,c, Fig. 6a-d, Supplementary Fig. 1d,g-i, Supplementary Fig. 2b, Supplementary Fig. 3c,d, Supplementary Fig. 5d,e,g and Supplementary Fig. 6a-d reported in this study are provided as supplementary source data tables in Supplementary Table 12. All other data supporting the findings of this study are available from the corresponding authors on reasonable request. Unique biological materials can be made available to third parties depending on research goals (i.e. absence of conflict of interest), mutual ethical permissions and Material Transfer Agreement.

Field-specific reporting

Please select the one below that is the best fit for your research. If you are not sure, read the appropriate sections before making your selection.

☒ Life sciences ☐ Behavioural & social sciences ☐ Ecological, evolutionary & environmental sciences

For a reference copy of the document with all sections, see nature.com/documents/nr-reporting-summary-flat.pdf

Life sciences study design

All studies must disclose on these points even when the disclosure is negative.

Sample size	Given the biobanking purpose of this study we tried to collect as many clinical samples as possible from all the different conditions (pathological conditions, grades and stages) and derive organoids from these samples. Given the descriptive nature of the paper we included at least 3 biological replicates (i.e. independent donors) per condition. When 5 or more samples per condition were available we performed the experiments with at least 5 independent donor lines (each performed with 3 technical replicates), sufficient to draw general conclusions about organoid behavior. When 3 donor lines per condition were available per experimental procedure (see ECT-O stage I and IV) we included all lines for the subsequent analyses. We did not statistically determine the sample size because the primary purpose of the study was to develop and describe a new in vitro organoid model for endometrium pathologies.
Data exclusions	No data were excluded from the analyses.
Replication	All experiments were performed with at least 3 biological replicates (i.e. independent donors) and were performed with 3 technical replicates per donor. In addition, different researchers were able to derive organoids with the described methodology with reproducible results (M. Boretto, L. Perneel, B. Bui, R. Heremans, N. Maenhoudt).
Randomization	Samples for establishing the organoids and performing the analyses were randomized per endometrium condition, depending on availability and time point of collection.
Blinding	Blinding was not relevant for this study since the scope was the development and characterization of organoids for different individual endometrium pathologies.

Reporting for specific materials, systems and methods

We require information from authors about some types of materials, experimental systems and methods used in many studies. Here, indicate whether each material, system or method listed is relevant to your study. If you are not sure if a list item applies to your research, read the appropriate section before selecting a response.

Materials & experimental systems

n/a	Involved in the study
<input type="checkbox"/>	<input checked="" type="checkbox"/> Antibodies
<input type="checkbox"/>	<input checked="" type="checkbox"/> Eukaryotic cell lines
<input checked="" type="checkbox"/>	<input type="checkbox"/> Palaeontology
<input type="checkbox"/>	<input checked="" type="checkbox"/> Animals and other organisms
<input type="checkbox"/>	<input checked="" type="checkbox"/> Human research participants
<input type="checkbox"/>	<input checked="" type="checkbox"/> Clinical data

Methods

n/a	Involved in the study
<input checked="" type="checkbox"/>	<input type="checkbox"/> ChIP-seq
<input checked="" type="checkbox"/>	<input type="checkbox"/> Flow cytometry
<input checked="" type="checkbox"/>	<input type="checkbox"/> MRI-based neuroimaging

Antibodies

Antibodies used

The antibodies used in this study are reported in Supplementary Table 10 with the appropriate specifications. The following antibodies were used against acetylated- α tubulin (mouse monoclonal, 6-11-b-1, Sigma Aldrich, 1/300, T7451), E-cadherin (rabbit monoclonal 24-E-10, Cell Signaling 1/400, 3195), Estrogen receptor alpha (rabbit polyclonal, EP1, Dako, ready-to-use), Progesterone receptor (mouse monoclonal PGR636, Dako, ready-to-use), Ki67 (MKI67) (rabbit polyclonal, NB500-170, Novus Biologicals, 1/100, 170SS), Pancytokeratin (mouse monoclonal, AE1/AE3, Dako, ready-to-use), Vimentin (mouse monoclonal, V9, Dako, ready-to-use), P53 (mouse monoclonal, DO-7, Dako, ready-to-use), P63 (rabbit monoclonal, D2K8X, Cell Signaling, 1/800, 13109), MSH6 (rabbit monoclonal, EP49, Dako, ready-to-use), MLH1 (mouse monoclonal, ES05, Dako, ready-to-use), Laminin-gamma1 (rabbit polyclonal, NB300, Novus Biologicals, 1/200, 144SS), B-catenin (mouse monoclonal, 610153, BD Transduction Laboratories, 1/500, 610153), MMP2 (mouse monoclonal, ab-37150, Abcam, 1/200), MMP7 (rabbit polyclonal, ab-5706, Abcam, 1/40) and PTEN (rabbit polyclonal, ab31392, Abcam, 1/500). As secondary antibody, horseradish peroxidase (HRP)-conjugated secondary antibody (ImmPRESS HRP universal antibody peroxidase-conjugated horse anti-mouse IgG/anti-rabbit IgG polymer detection kit; MP-7500, Vector Laboratories) was used. Sections were counterstained with hematoxylin. Periodic Acid Schiff (PAS) staining was performed to visualize mucin according to manufacturer instructions (395B-1KT, Sigma Aldrich). Secondary antibodies used in the study include Donkey anti-rabbit IgG (H+L) (alexafuor 555, A31572, 1866859, 1/500, Thermo Fisher Scientific), Donkey anti-mouse IgG (H+L) (alexafuor 555, A31570, 2045336, 1/500, Thermo Fisher Scientific), Donkey anti-rabbit IgG (H+L) (alexafuor 488, A21206, 1927937, 1/500, Thermo Fisher Scientific) and Donkey anti-mouse IgG (H+L) (alexafuor 488, A21202, 1915874, 1/500, Thermo Fisher Scientific).

Validation

Ready-to-use Dako-produced antibodies were received from the pathological laboratory and are routinely used for pathological evaluation of surgical human specimens for diagnostic purposes. All other antibodies were validated by omitting the primary antibody during the immunohistochemical process in which case no staining was observed. Positive and negative control samples were included for validation.

Acetylated- α tubulin (validated reactivity against monkey, protista, mouse, pig, human, bovine, invertebrates, rat, hamster, plant, frog, chicken. Relevant publication has been listed on the website company page of the product together with a certificate of analysis). E-cadherin (validated reactivity against human and mouse. Relevant publication has been listed on the website company page of the product together with a certificate of analysis). Estrogen receptor alpha (validated reactivity against human. The antibody is routinely used in clinics for diagnostic purposes. Relevant publication has been listed on the website company page of the product together with a certificate of analysis). Progesterone receptor (validated reactivity against human. The antibody is routinely used in clinics for diagnostic purposes. Relevant publication has been listed on the website company page of the product together with a certificate of analysis). Ki67 (MKI67) (validated reactivity against human, mouse, rat, porcine. Relevant publication has been listed on the website company page of the product together with a certificate of analysis). Pancytokeratin (validated reactivity against mouse and human. The antibody is routinely used in clinics for diagnostic purposes. Relevant publication has been listed on the website company page of the product together with a certificate of analysis). Vimentin (validated reactivity against human. The antibody is routinely used in clinics for diagnostic purposes. Relevant publication has been listed on the website company page of the product together with a certificate of analysis). P53 (validated reactivity against human. The antibody is routinely used in clinics for diagnostic purposes. Relevant publication has been listed on the website company page of the product together with a certificate of analysis). P63 (validated reactivity against human. Relevant publication has been listed on the website company page of the product together with a certificate of analysis together with a certificate of analysis). MSH6 (validated reactivity against human. The antibody is routinely used in clinics for diagnostic purposes. Relevant publication has been listed on the website company page of the product together with a certificate of analysis). MLH1 (validated reactivity against human. The antibody is routinely used in clinics for diagnostic purposes. Relevant publication has been listed on the website company page of the product together with a certificate of analysis). Laminin-gamma1 (validated reactivity against human, mouse, rat, chinese hamster, rabbit. Relevant publication has been listed on the website company page of the product together with a certificate of analysis). B-catenin (validated reactivity against human, mouse, rat, dog, chicken. Relevant publication has been listed on the website company page of the product together with a certificate of analysis). MMP2 (validated reactivity against human, mouse, rat, chicken. Relevant publication has been listed on the website company page of the product together with a certificate of analysis). MMP7 (validated reactivity against human, mouse. Relevant publication has been listed on the website company page of the product together with a certificate of analysis). PTEN (validated reactivity against human, mouse and rat. Relevant publication has been listed on the website company page of the product together with a certificate of analysis), Donkey anti-rabbit IgG (H+L) (alexafuor 555, relevant information about validation are present on the datasheet of the manufacturer), Donkey anti-mouse IgG (H+L) (alexafuor 555, relevant information about validation are present on the datasheet of the manufacturer), Donkey anti-rabbit IgG (H+L) (alexafuor 488, relevant information about validation are present on the datasheet of the manufacturer) and Donkey anti-mouse IgG (H+L) (alexafuor 488, relevant information about validation are present on the datasheet of the manufacturer).

Eukaryotic cell lines

Policy information about [cell lines](#)

Cell line source(s)	HEC-1a cell line was originally obtained from ATCC (LGC Standards, Teddington, UK) as reported in the manuscript.
Authentication	The cell line used was not authenticated but shows clear endometrial cancer characteristics compatible with a poorly differentiated adenocarcinoma after in vivo growth, as reported on the ATCC website.
Mycoplasma contamination	The HeC-1a cell line as well as the organoid cultures were regularly tested and found negative for mycoplasma contamination.
Commonly misidentified lines (See ICLAC register)	No commonly misidentified lines were used.

Animals and other organisms

Policy information about [studies involving animals](#); [ARRIVE guidelines](#) recommended for reporting animal research

Laboratory animals	NOD/SCID female mice of 6-12 weeks were used for this study.
Wild animals	No wild animals were included in the study.
Field-collected samples	No field-collected samples were included in the study.
Ethics oversight	Mouse experiments were approved by the KU Leuven Ethical Committee for Experimental Animals; this statement is included in the Methods section.

Note that full information on the approval of the study protocol must also be provided in the manuscript.

Human research participants

Policy information about [studies involving human research participants](#)

Population characteristics	Human participants involved in the study were women affected by endometrial pathologies and healthy donors. The population was heterogeneous for age (ranging from pre-menopausal to post-menopausal women), menstrual cycle phase (proliferative, secretory or under hormonal contraceptive; information included in Supplementary Table 1), ethnicity and diagnosis of endometrial disease (endometriosis from all representative stages, hyperplasia of all representative subtypes and endometrial low/high grade cancer; information included in Supplementary Table 1).
Recruitment	Human participants were recruited on the basis of endometrial diseases. Participants were excluded if positive for bacterial or viral infection. All other participants were included in the study and no selection criteria (other than the presence of endometrial diseases) were applied that could have biased the results. Endometrial biopsies from healthy donors were obtained and used to compare the results obtained for diseased endometrium. Also here, no selection was applied and biopsies were obtained from different menstrual phases (as described in Supplementary Table 1). Participants provided informed consent; this statement is included in the Methods section.
Ethics oversight	The study was approved by the Ethical Committee Research UZ/KU Leuven (S59006; S59177) and is compliant with all relevant ethical regulations regarding research involving human participants. This statement is included in the Methods section.

Note that full information on the approval of the study protocol must also be provided in the manuscript.

Clinical data

Policy information about [clinical studies](#)

All manuscripts should comply with the ICMJE [guidelines for publication of clinical research](#) and a completed [CONSORT checklist](#) must be included with all submissions.

Clinical trial registration	No clinical trial was performed.
Study protocol	The study protocol for obtaining the clinical samples was approved by the Ethical Committee Research UZ/KU Leuven (S59006; S59177). The protocol to derive organoids from the collected biopsies is described in the Methods section and a more detailed protocol is available on request.
Data collection	Clinical information about the patients was collected for correlation with organoid establishment and characteristics (included in Supplementary Table 1).
Outcomes	NA